

PROTOTYPE OF A HAND-HELD RF DOSIMETER BASED  
ON 8-BIT PROCESSOR AND AN INTEGRATED  
TEMPERATURE SENSOR

By

REGHU K. RAJAN

Bachelor of Science

Cochin University of Science and Technology

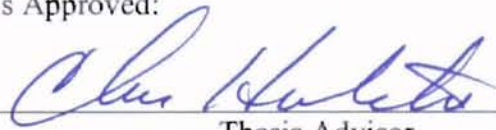
Cochin, India

1996

Submitted to the Faculty of the  
Graduate College of the  
Oklahoma State University  
in partial fulfillment of  
the requirements for  
the Degree of  
MASTER OF SCIENCE  
August, 2001

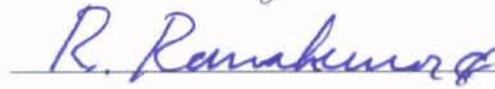
PROTOTYPE OF A HAND-HELD RF DOSIMETER BASED  
ON 8-BIT PROCESSOR AND AN INTEGRATED  
TEMPERATURE SENSOR


Thesis Approved:

  
\_\_\_\_\_

Thesis Advisor

  
\_\_\_\_\_

  
\_\_\_\_\_

  
\_\_\_\_\_

Dean of the Graduate College

## ACKNOWLEDGEMENTS

I wish to express my gratitude and appreciation to Dr. Chris Hutchens for providing me the technical guidance and encouragement throughout my studies. I wouldn't be the same if I hadn't been in his research group. I also thank him for all the personal guidance and support given to me, both academic and otherwise. My sincere appreciation extends to my other committee members Dr. Louis G. Johnson and Dr. Rama Ramakumar for the help and support on this effort.

I thank my parents and sister for being with me in my life, encourage, tolerate and for all the love and understanding.

Moreover, I wish to express my sincere gratitude to all my colleagues and friends for their help and support in my effort and also for this study. I thank you all.

Finally I thank SPAWAR Systems Center, San Diego and Titan Corporation, San Diego for the support, funding and giving me opportunity to use the facility in site. I also thank the staff of Department of Electrical and Computer Engineering of Oklahoma State University for my Master's degree.

## TABLE OF CONTENTS

Chapter	Page
1. INTRODUCTION.....	1
1.1 Objective.....	2
1.2 Organization.....	2
2. DOSIMETER OVERVIEW.....	4
2.1 Effects of RF energy on human body.....	4
2.2 Dosimeter for defense application.....	6
2.3 Dosimeter requirements.....	7
2.4 System level of dosimeter.....	8
3. PROTOTYPE OF DOSIMETER - HARDWARE AND SOFTWARE.....	10
3.1 Prototype overview.....	10
3.2 Daughter board and RF sensors.....	11
3.2.1 Thermopile based RF detectors.....	13
3.2.2 Active sensors.....	16
3.3 Hardware and interface.....	14
3.3.1 Circuit overview.....	15
3.3.2 Daughter board interface.....	15
3.3.3 Analog amplifier section.....	18
3.4 CPU and peripherals.....	21
3.5 Liquid crystal interface.....	22
3.6 Power management.....	22
3.7 User interface.....	23
3.7.1 Main page.....	23
3.7.2 RF level display page.....	23
3.7.3 Battery level display page.....	25
3.7.4 Program mode.....	27
3.8 Alarms.....	29
3.8.1 Low battery alarms.....	29
3.8.2 RF level alarms.....	29
3.9 Software.....	31
3.9.1 Main loop.....	31
3.9.2 Logic control subroutine.....	33
3.9.3 Automatic gain control.....	33

Chapter	Page
3.10 Adjusting software parameters.....	34
3.10.1 Changing low-battery alarm setting.....	35
3.10.2 Changing RF-power alarm levels.....	36
4 INTEGRATED TEMPERATURE SENSOR.....	37
4.1 Principle of PN junction temperature sensor.....	38
4.1.1 Switched-current linearizing.....	39
4.2 Circuit and diode implementation.....	40
4.3 Self heating error analysis.....	43
4.4 Test results of fabrication.....	45
4.3.1 Diode Curves.....	45
4.3.2 Current mirror tests.....	47
4.3.3 Sensor tests.....	49
5. CONCLUSION.....	53
REFERENCES.....	56
APPENDIX A-- Dosimeter Circuits and Design.....	60
Vita.....	66

## LIST OF TABLES

Table	Page
3.1 Frequency response of various antennae.....	12
3.2 Interface pins to daughter board.....	16
3.3 Input ranges for different gain levels.....	18
3.4 Gain levels versus full scale input.....	24
3.5 Block of code from line 38 through 40 in the source code.....	35
3.5 RF Alarm setting.....	36

## LIST OF FIGURES

Figure	Page
2.1 FCC exposure guidelines for RF exposure.....	5
2.2 Power distribution of RF spectrum.....	6
2.3 Block level of RF dosimeter.....	9
3.1 Antenna and thermopile.....	11
3.2 Layout of thermopile.....	12
3.3 Layout of bowtie antenna.....	13
3.4 Layout of flare antenna.....	13
3.5 Block diagram of prototype motherboard.....	15
3.6 Block diagram of daughter board with thermopile sensor.....	17
3.7 Amplifier gain curve (a,b,c,d).....	19, 20, 21
3.8 Main page display.....	23
3.9 RF Level display page.....	24
3.10 Battery level display page.....	25
3.11 Low battery warning page.....	25
3.12 Over voltage warning page.....	26
3.13 Flow of events in 'Run' mode.....	27
3.14 Flow of events in 'Program' mode.....	28
3.15 Low battery alarm pattern.....	29
3.16 RF Level alarm pattern.....	30

Figure	Page
3.17 Main algorithm.....	32
3.18 Automatic gain control.....	34
4.1 Implementation of sensor diode on the substrate.....	41
4.2 Implementation of temperature sensor .....	42
4.3 Layout of temperature sensor on AMI 1.2 micron process.....	45
4.4 Log-linear curve of the sensor diode.....	46
4.5 Current mirror plot at $55\mu\text{A}$ .....	47
4.6 20x Current mirror plot at $55\mu\text{A}$ .....	48
4.7 Test setup of temperature sensor.....	49
4.8 Temperature sensor characteristics.....	50
4.9 Error plot from least-fit-curve analysis.....	51
4.10 Comparison of actual versus theoretical sensor curve.....	52



## NOMENCLATURE

AAF	Anti-aliasing filter
ADC	Analog-to-digital converter
AMI	American Microsystem Incorporation
$A_v$	OTA open-loop gain
$C_{gs}$	Gate to Source Capacitance of Transistor
$C_{db}$	Drain to Body Capacitance of Transistor
$C_L$	Load Capacitance
DAC	Digital-to-analog converter
DR	Dynamic range
$e$	Quantization error introduced in the $\Sigma\Delta$ loop
FFT	Fast Fourier Transform
$f_N$	Nyquist frequency in hertz
$f_s$	Sample frequency in hertz
HHPM	Hand held power meterp
$I_d$	Forward diode of diode
$I_s$	Reverse saturation current
$k$	Boltzmann's constant
KSPS	Kilo sample per second
MOSFET	Metal-Oxide-Semiconductor Field-Effect-Transistor
NTF	Noise transfer function
OSR	Oversampling ratio
OTA	Operational Transconductance Amplifier
SNR	Signal to Noise Ratio
$P$	Average noise power
$q$	Electron charge ( $1.6 \times 10^{-19}$ Coulombs)

$g_m$	Transconductance Parameter
$g_{ds}$	Drain to Source Transconductance Parameter
$t_{ox}$	Thickness of Oxide Layer
$V_{DS}$	MOSFET drain to Source Voltage
$V_{GS}$	MOSFET gate to Source Voltage
$V_{IH}$	Minimum Input High Voltage
$V_{IL}$	Maximum Input Low Voltage
$V_T$	Thermal voltage
$W$	Channel Width of Transistor
$W_{eff}$	Effective Channel width of Transistor
$x$	Input to $\Sigma\Delta$ loop
$y$	Output signal of modulator
PCB	Printed Circuit Board
CTR	Current transfer ratio
LCD	Liquid crystal display

## CHAPTER 1

### INTRODUCTION

From the modern business world to the battle field man is exposed to a haze of radio waves. The communication revolution makes it possible for every person to carry of RF device and has made virtually all communication wireless. The steady growth of integration technology has resulted in improvement of more compact and powerful RF devices. The military also relies heavily on RF equipment for communication and surveillance. This has led to the need to measure ambient RF power levels including the monitoring of human exposure to RF radiation from the flight deck of a carrier to a radio officer or a soldier on the ground. The dosimeter finds a wide range of applications from; 1) the study of the effects of long term exposure of human subjects at various frequencies of RF spectrum with varying power levels; 2) as a detector to sense enemy surveillance and 3) as a health monitor to warn presence of dangerous levels of RF fields. The recent advancement in semiconductor technology and MEMS research has fueled this project to develop a single chip solution for RF sensing and power measurement.

The long-term goal of the dosimeter project funded by SPAWAR (Space and Naval warfare Systems Center) in a joined effort with Titan Corporation Inc, San Diego, is to develop a hand-held RF dosimeter based on a single chip for RF sensor and processor.

## 1.1 Objective

The first objective of this thesis, apart from discussing the scope of RF dosimetry and various antennae, is to present the design and development of a dosimeter prototype that forms a platform for demonstration and development of the integrated version. The second objective of this thesis is to document the effort to develop an integrated temperature sensor and RF power detector based on a single PN junction.

The study begins with a review on RF dosimetry and the various applications. This covers the range of frequencies of interest and power levels and the specific application. A brief study of various sensors and antennae is also presented. The dosimeter prototype consists of a daughter board and motherboard. The daughter board houses various antennae. The motherboard consists of analog amplifiers and an 8-bit processor with ADC. The body of thesis explains the hardware, software and features of the prototype.

The PN junction based temperature sensor incorporates a technique to achieve linearity by a method of switched currents to eliminate the effects of reverse saturation current [20]. The sensor has been successfully fabricated on a commercial 1.2-micron process and the results are documented. This sensor finds use in substrate temperature measurements and also as a transducer to measure temperature-independent RF power.

## 1.2 Organization

Chapter 1 introduces the background and the purpose for this study.

Chapter 2 discusses the scope of the device in terms of possible applications, RF spectrum and power levels of interest, various antennas and possible signal levels anticipated from these sensors. A block level organization of the dosimeter and functions of various sections are presented.

Chapters 3 discuss in detail the circuit and interface for the sensor with the controller through the amplifier and presents the details of the motherboard design. The assembly level software is also documented with flow charts of each function and subroutine. The layout issues of the PCB are also presented.

Chapter 4 presents the design and results of the integrated temperature sensor. The theory of operation, design and layout is discussed. Issues related to error from self-heating are discussed and analyzed. Finally the results from a fabrication run are presented.

Chapter 5 summarizes the results of this study, conclusions, and proposes some improvements.

## CHAPTER 2

### DOSIMETER OVERVIEW

An RF Dosimeter finds application where RF radiation exposure needs to be detected and/or recorded. The main functions of a dosimeter are to record strength of the field, frequency of exposure, exposure profile (field strength versus time plot) and alert the user with audio-visual alarms. This chapter describes some dosimeter applications and concludes with the specifications required for RF dosimeter.

#### 2.1 Effects of RF Energy on biological matter.

Effects of human exposure to RF radiation became a concern with the extensive use of radars on ships during the post world-war II years. Research has been conducted to study human absorption of RF radiation [12][13]. No scientific study has proven a link between common RF radiation and any human body disorder like cancer; however, extreme power levels of RF radiations are linked with biological tissue heating, which primarily results in cataracts of the eyes. Effects of RF radiation on biological cells and DNA are not fully understood to date. Recent popularity of cell phones has raised concerns about links of cell phone usage with cancer [14], again to date, no research has proven any link. Studies have been conducted to determine human tissue heating due

close proximity of cell phones and possible links to any medical disorders [32]. The human body shows maximum absorption to frequencies in the range 30 to 300 MHz [21]. Water, fat and certain hydrocarbon molecules in biological tissues absorb RF energy. The absorption results in heating up of the matter. This can result in permanent or reversible changes to the tissues. The extend of heating and damage depends on the intensity of RF energy, time of exposure and frequency of radiation (absorption varies across the spectrum). The FCC has adopted exposure guidelines to limit human exposure to RF energy based on the absorption spectrum of biological tissues [13]. The guidelines are based on the intensity and frequency (see Figure 2.1)

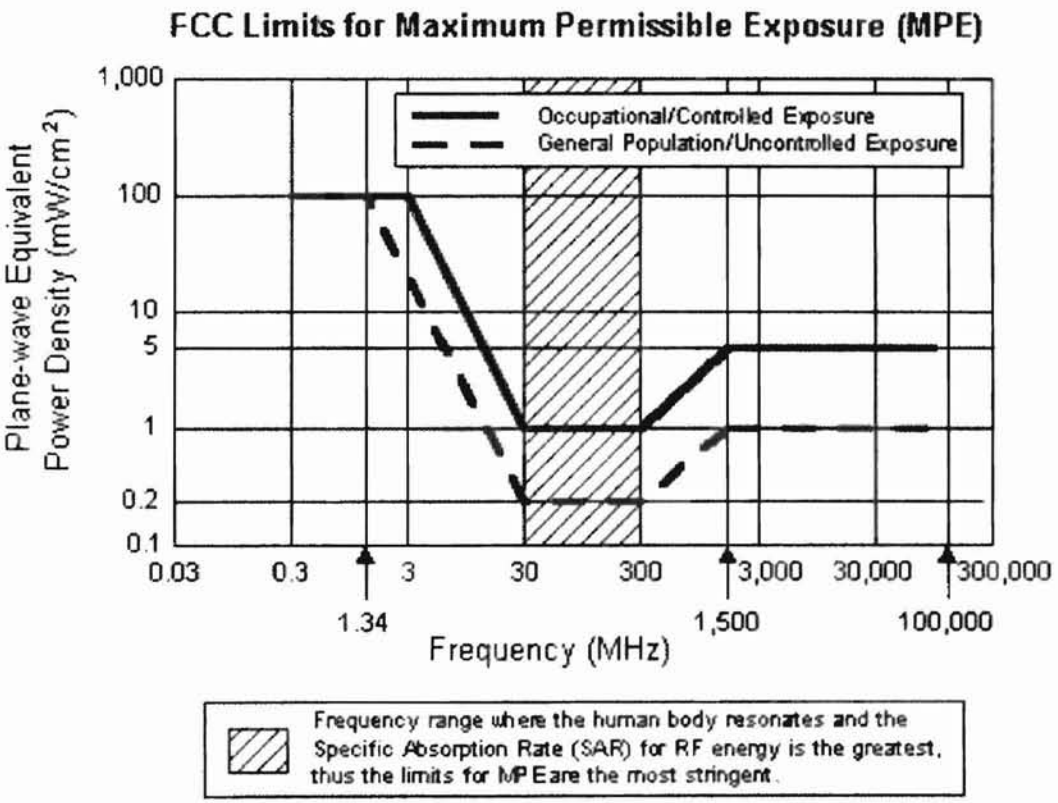


Figure 2.1 FCC exposure guidelines for RF exposure

## 2.2 Dosimeter for Defense Application

As mentioned in the previous chapter, RF Dosimeter finds immense application in the military. For example an aircraft carrier deck has several RF sources including powerful communication antenna network, radar antennae (high power microwave transmitters on board both ship and aircraft), internal communication radios for deck personnel and the pilot and yet-to-be-developed wireless communication. Figure 2.2 shows typical power levels of various bands in the RF spectrum [21].

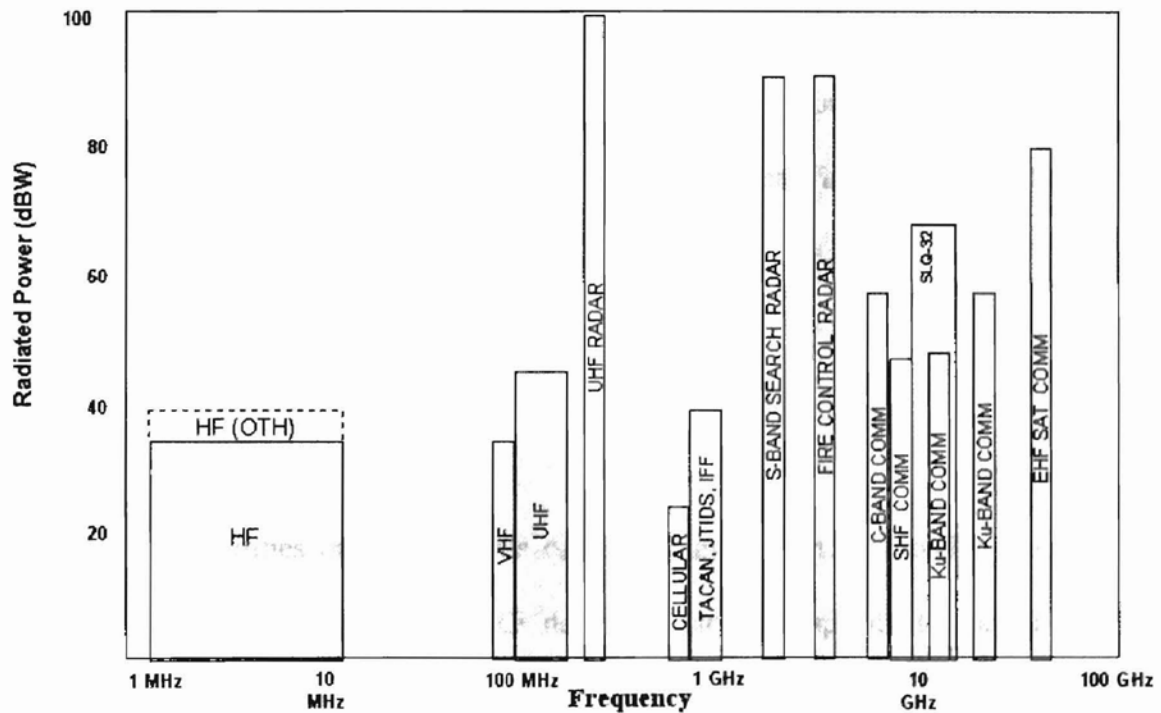


Figure 2.2 Power distribution of RF spectrum

From figure 2.2, it can be seen that maximum power levels are emitted from Radar antennae. Most defense sites, if not all, have radars installed (War-ships, Fighter



aircrafts, battle field, tanks etc). This makes a low cost dosimeter an essential safety device for all military personnel.

Apart from the dosimeter application, RF sensors have applications as detectors. RF fields need to be detected to make troupe aware of presence of enemy surveillance and detect radio jammers. Miniature detectors allow soldiers, ships and fighter crafts to know when enemy radars patch or jam them. Other applications are to sense RF leakage from damaged communication devices or cable joints and for setting up antenna directivity. Modification or replacement of the sensor enables detection of other types of radiation (for example, ionizing radiation from a reactor). RF sensors also find application to detect timed explosives that have clocked electronics. This finds potential application in civil aviation and for the prevention of terrorism. All clocked electronic devices emit short range RF radiation. A portable RF detector has the potential to locate hidden timed explosives.

### 2.3 Dosimeter requirements

The capabilities or requirements of the dosimeter can be broadly classified as functional capabilities in terms of; RF detection, storage capacity to record and log exposure data for transfer to host a computer, audio-visual warnings and built-in diagnostics.

The RF specification required for the proposed dosimeter is shown in figure 2.1 and 2.2. The functional capability of the dosimeter includes band limited RF power measurement in the frequency range of 3MHz to 45 GHz with a sensitivity of 0.2mW/ sq.

cm to 2W/sq. cm. Other features of the dosimeter are to compute average incident power, exposure profile and user warnings and alarms. The next section discusses a block level approach to the design of a dosimeter to meet these specifications.

#### 2.4 System Level of Dosimeter

The front end of the dosimeter is the RF sensor used to detect the power level of incident radiation across the entire spectrum of interest. As mentioned earlier, the working spectrum of the dosimeter ranges from 3MHz to 45MHz. This requires several types of sensor antennae since one antenna cannot sense the entire spectrum of interest. The various types of sensors and their frequency response are detailed in the next section. Figure 2.3 shows the system level blocks of the dosimeter. The sensor returns voltages proportional to the RF power [21]. A multistage variable-gain amplifier with anti aliasing filter amplifies the signal. The ADC digitizes the amplified signal.

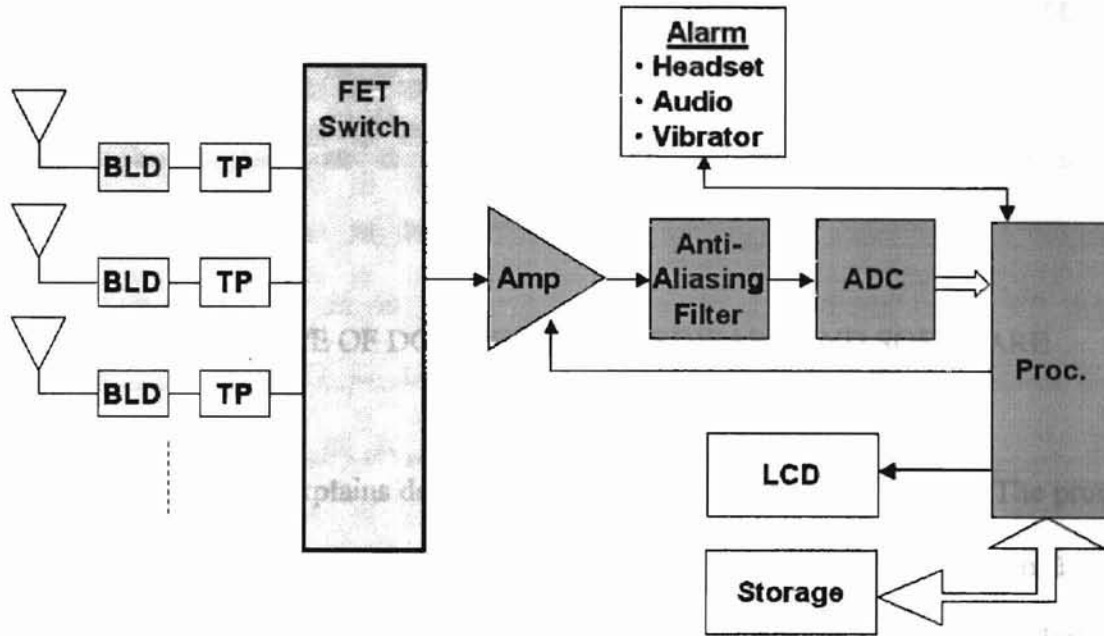


Figure 2.3 Block level of RF Dosimeter.

The CPU processes the digital data to compute average RF power, peak levels and exposure data. Various warning and alarms are triggered at programmed levels. On board memory is required to store the power level data for the recorded exposure profile and averages. The averaging time constants required take on values from 100mS to 1 minute [21]. The sampling rate and profile time sets the memory capacity for exposure profile. The required modes of sampling are a daily profile mode with a sample rate of one per second and weekly/monthly profile with the sample rate of one per minute [21]. The CPU also controls user-warning devices like liquid-crystal display and audio alarms. The next chapter describes in detail the design of the hardware and software of the dosimeter prototype and sensors.

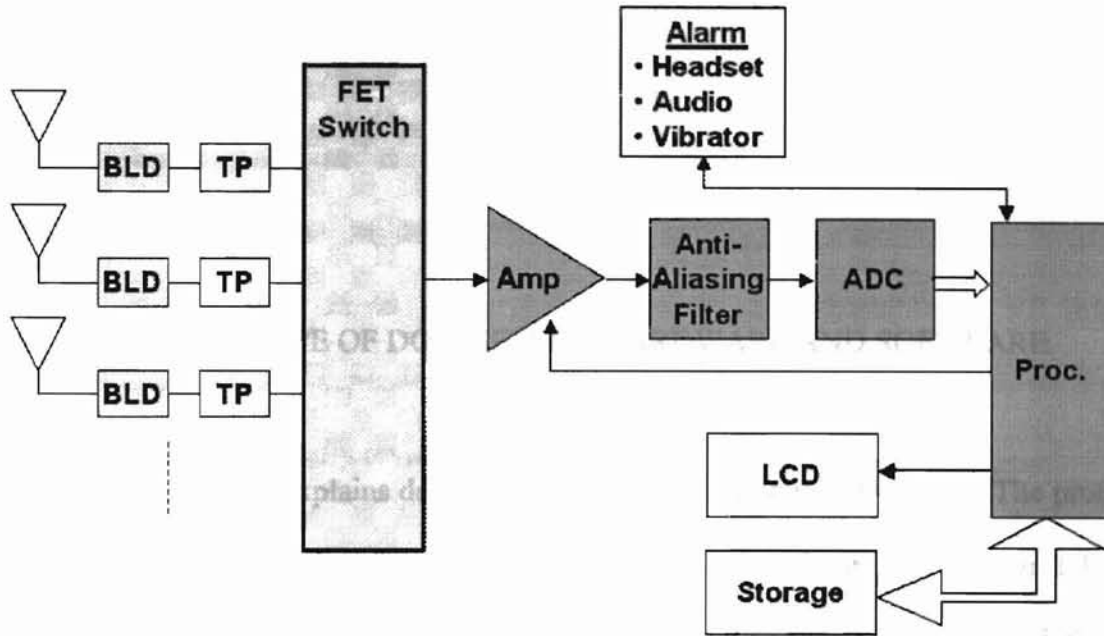


Figure 2.3 Block level of RF Dosimeter.

The CPU processes the digital data to compute average RF power, peak levels and exposure data. Various warning and alarms are triggered at programmed levels. On board memory is required to store the power level data for the recorded exposure profile and averages. The averaging time constants required take on values from 100mS to 1 minute [21]. The sampling rate and profile time sets the memory capacity for exposure profile. The required modes of sampling are a daily profile mode with a sample rate of one per second and weekly/monthly profile with the sample rate of one per minute [21]. The CPU also controls user-warning devices like liquid-crystal display and audio alarms. The next chapter describes in detail the design of the hardware and software of the dosimeter prototype and sensors.

## CHAPTER 3

### PROTOTYPE OF DOSIMETER – HARDWARE AND SOFTWARE

This chapter explains details of the design for prototype dosimeter. The prototype “Hand Held Power Meter” (HHPM), with embedded software, is version 1.1. This chapter begins with a review of the daughter board and various sensors. This defines the requirements for the amplifier on the motherboard and the rest of the hardware. Finally, the user interface is explained with flow chart of screen displays and device operation. The chapter concludes with the explanation of internal algorithm and embedded firmware implementation.

#### 3.1 Prototype Overview

The HHPM prototype board is a fully programmable piece of hardware, which can support multiple sensors on a daughter board. The main board is designed to provide a standard interface that can accommodate multiple daughter boards with various types of sensors with little or no change in the hardware or software.

### 3.2 Daughter board and RF sensors

frequencies (2MHz to 45

physical structure to

The daughter board carries one or more of the RF sensor(s). Several types of RF transducers have been considered. The sensors are broadly classified into thermopile-based detectors and active-element based detector, i.e., diode based RF detector. Daughter boards are dependent on the main board for power and control signals. Following sections briefly reviews various sensors.

#### 3.2.1 Thermopile based RF detectors

This classification of detectors consists of antennae elements to pick the RF. The energy from the antenna is dissipated on a resistor, which forms a matched impedance [18]. The rise in temperature of this resistor is measured using a thermo-couple bank, which produces a voltage proportional to the difference in the temperature of 50 Ohm resistor and the substrate (Seebeck effect) [21]. This voltage is a measure of RF power collected by the antenna. Basic architecture of a thermopile sensor is shown in figure 3.1.

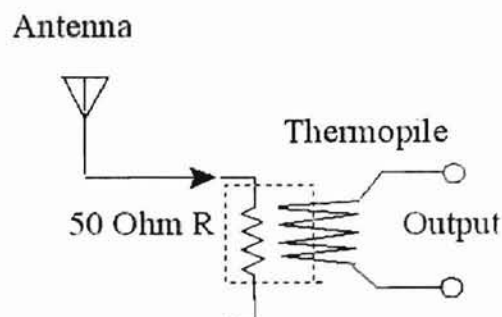


Figure 3.1 Antenna and thermopile

Since the RF spectrum of interest covers a wide range of frequencies (2MHz to 45 GHz), several types of antennae have been proposed with changes in physical structure to cover the entire spectrum with little overlap of bandwidth. Table 3.1 shows the frequency bins of various types of antennae. A daughter board can house several of these and the outputs are multiplexed for sampling under the control of the processor.

Type of Antenna	Frequency Range
Flare Antenna (1)	20 GHz – 100 GHz
Bowtie Antenna (1)	8 GHz – 20 GHz
Bowtie Antenna (2)	2 GHz – 8 GHz
Flare Antenna (2)	0.5 GHz – 2 GHz
Spiral Antenna (Off Chip)	100 MHz – 0.5GHz
Loop Antenna (Off Chip)	2 MHz – 100 MHz

Table 3.1 Frequency responses of various antennae

A sample layout of the thermopile coupled with the 50Ω block is shown in figure 3.2.

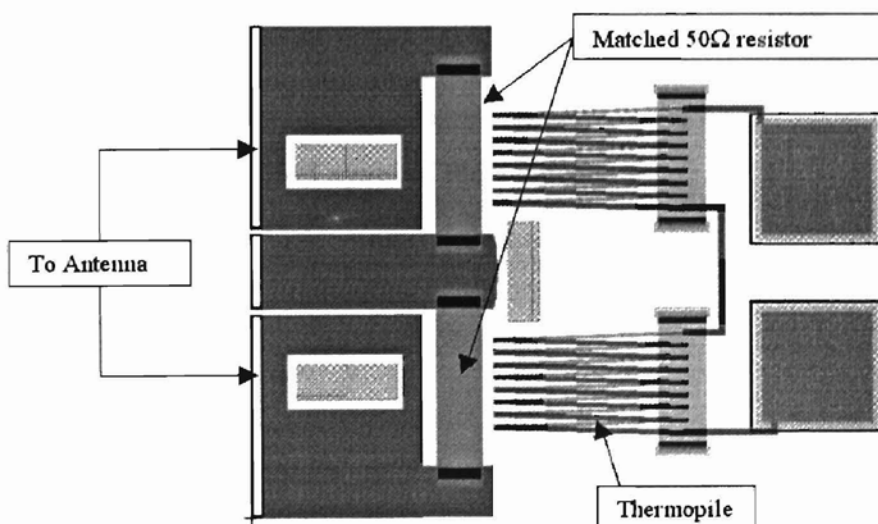


Figure 3.2 Layout of thermopile and 50Ω resistor

Various micro-machined antennae developed at the Berkeley sensor group [22] include the bow-tie and flare structures shown in figure 3.3 and 3.4.

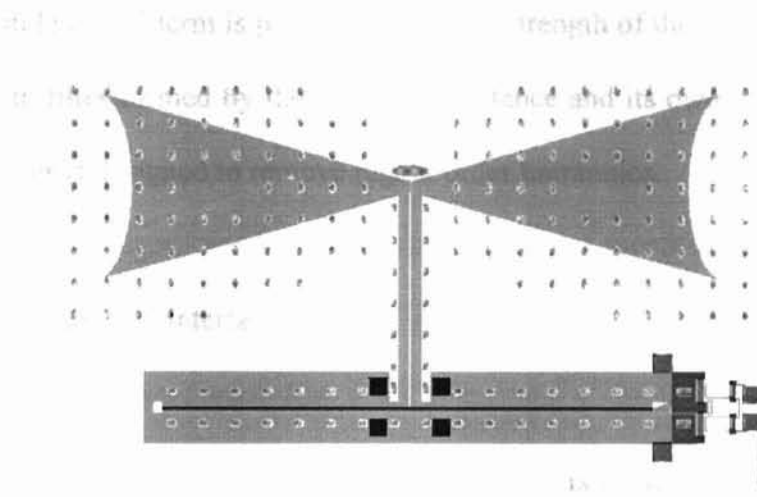


Figure 3.3 Layout of Bowtie antenna

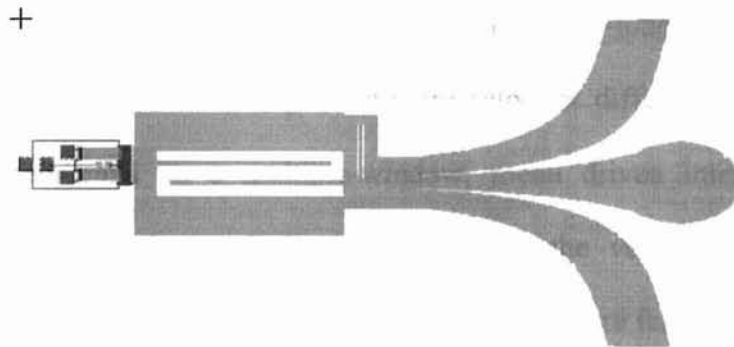


Figure 3.4 Layout of Flare antenna

### 3.2.2 Active sensors

The active sensors exploit the nonlinear voltage-current characteristics of semiconductor devices, PN junctions or a MOSFET to rectify high frequency RF signals to a DC signal and its harmonics [39]. When RF is applied to a PN junction, the nonlinear



characteristics of the device, transforms the RF voltage waveform into a series of harmonics with a DC term. If the harmonics are filtered out using a suitable filter, the amplitude of DC term is proportional to the strength of the incident RF. In addition to the intrinsic filter formed by the device capacitance and its own impedance, an external low pass filter is designed to remove higher order harmonics.

### 3.3 Hardware and interface

The primary function of the main board is to digitize and monitor the amplified signals from the sensors on the daughter board. The main board has an analog front-end for signal amplification. An 8-bit micro-controller controls the entire system. User-interface includes a 16x2 matrix Liquid-crystal display, mono-tone buzzer and two micro push-switches. The various warning alarms are setoff at different programmable RF levels. The system runs on a multiple-window, menu driven interface. The 'User Interface' section of the manual describes in detail the various software features. Software has provisions for future upgrades to incorporate more features and functions.

The hardware on the prototype motherboard is built around discrete components and broadly separated as analog front-end, digital back-end including CPU, display and user interface and power management.

### 3.3.1 Circuit overview

The block diagram of the system is shown in figure 3.5. The sensors and multiplexer are on the daughter board. The rest of the circuit is on the main board. The PCB is laid out to separate analog and digital circuits to reduce clock noise. One side of the PCB has digital section comprising of micro-controller and DC-DC converters. The other side has analog amplifier and gain stages. Intermediate ground layers in the PCB reduces noise from digital side.

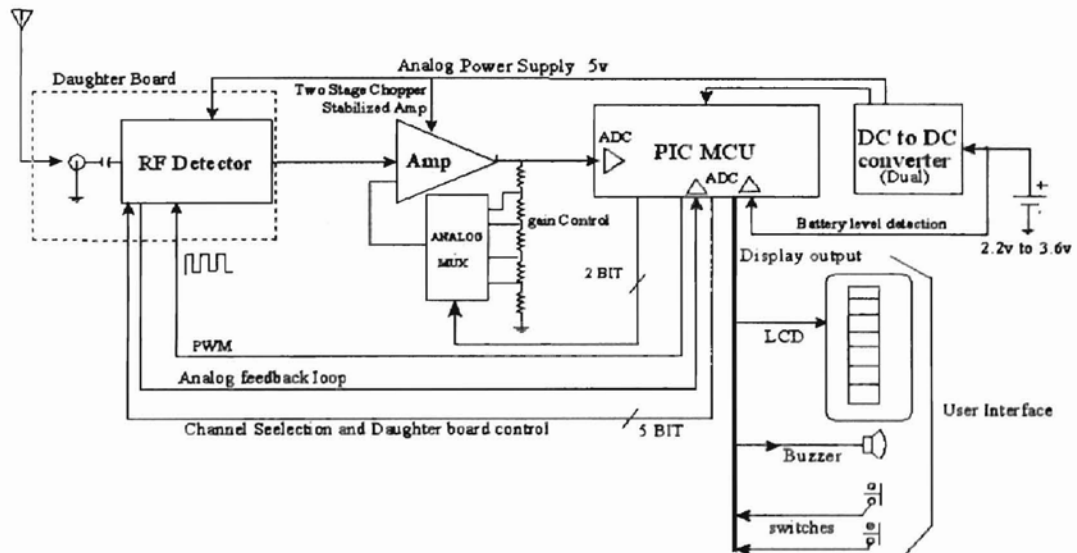


Figure 3.5 Block diagram of prototype motherboard

All the sections in the block diagram are explained in detail below.

### 3.3.2 Daughter board interface

The daughter board houses the RF sensor and antenna-selector switches. The daughter board is built on a ceramic substrate with gold lines for connectivity. This

enhances the RF performance due to superior dielectric properties and insulation of ceramic, which explains the reason to have a separate daughter board apart from the fact that several antennae can be tested on one motherboard. The list of pins that interface the daughter board to the motherboard is shown in table 3.2 with pin functions.

Pin #	Pin Name	Function
1	5V_A	5V Analog Vdd
2	Vout	Analog Voltage out for feed back loop
3	GND_A	Analog Ground
4	Vout+	Sensor output (+ve)
5	Vout-	Sensor output (-ve)
6	GND_A	Analog Ground
7	GND_D	Digital Ground
8	PWM1	Pulse Width Modulated stream from PIC CPU
9	5V_D	5 V Digital Vdd
10	CNTRL0	Digital I/O lines to CPU for control/sensing
11	CNTRL1	Digital I/O lines to CPU for control/sensing
12	CNTRL2	Digital I/O lines to CPU for control/sensing
13	CNTRL3	Digital I/O lines to CPU for control/sensing
14	CNTRL4	Digital I/O lines to CPU for control/sensing

Table 3.2 Interface pins to daughter board.

The interface pins to daughter board include power lines (both digital and analog) and signal lines. The sensitive signal lines from the RF sensor are ‘sandwiched’ with a pair of analog-ground for shielding to reduce noise. These signals are connected to the input of the amplifier. A PWM line and an analog feedback are provided from the controller to the daughter board. This is provided for future upgrades. These lines can be used for closed loop control on daughter board for auto-zeroing the RF sensor or removing ambient RF noise levels to boost the sensitivity of the selected RF spectrum.

The different MEMS antennae connected to integrated banks of thermocouple form the thermopile sensor. Several such thermopile sensors (spectrum specific antennae) tuned to specific bands of frequency can be housed on a daughter board. The output of sensors are multiplexed and fed to the input of the amplifier. The controller selects specific antenna by selecting the appropriate thermopile channel on the daughter board.

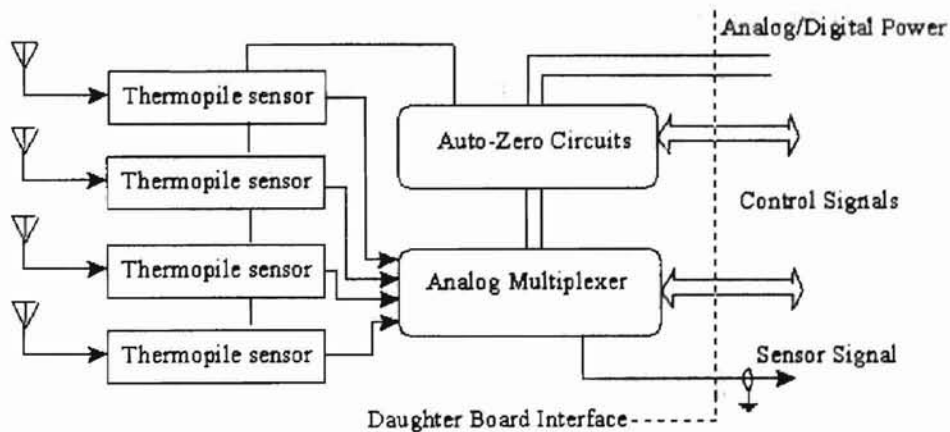


Figure 3.6 Block diagram of daughter board with thermopile sensor

The block diagram of daughter board is shown in figure 3.6. The controller sets control signals for multiplexer to select channels.

### 3.3.3 Analog amplifier section

The signal from the sensor is fed to an instrumentation amplifier built with TL4502 (Texas Instruments family of self-calibrating Operational Amplifier, See appendix for data sheet and design). The amplifier is designed in three stages. The first stage forms a high input-impedance stage. The gain of this stage is 50. The second stage merely eliminates the common mode gain of the first stage. The second stage is a unity gain configuration with low pass filter network designed with a cut-off frequency of 100Hz.

The third stage of the amplifier is a variable gain stage. An analog MUX is used to step the resistor network in the feedback loop of a non-inverting amplifier. The reader is referred to the appendix for circuit diagrams and design calculations. The CPU controls the MUX and gain is automatically set depending on the input signal level to achieve maximum resolution and range. The gain levels of the amplifier are 100, 200, 500 and 1000. The full-scale input voltage to the ADC on the controller is 5V. Table 3.3 shows the input range at various gain stages.

Gain	100	200	500	1000
Input range	0 – 50 mV	0 – 25 mV	0 – 10 mV	0 – 5 mV

Table 3.3 Input ranges for different gain levels.

The plots of test results of the amplifier gain are shown in figure 3.7 a,b,c&d.

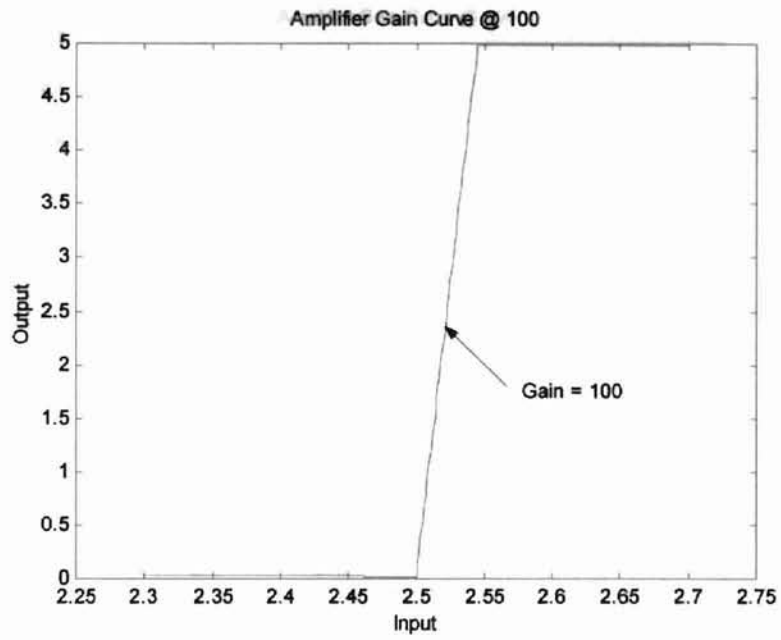


figure 3.7a Amplifier gain curve (Gain=100)

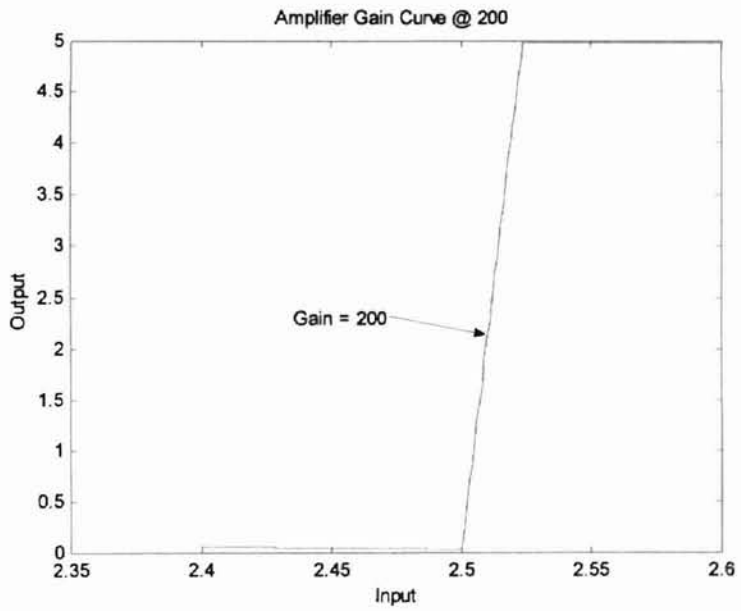


figure 3.7b Amplifier gain curve (Gain=200)

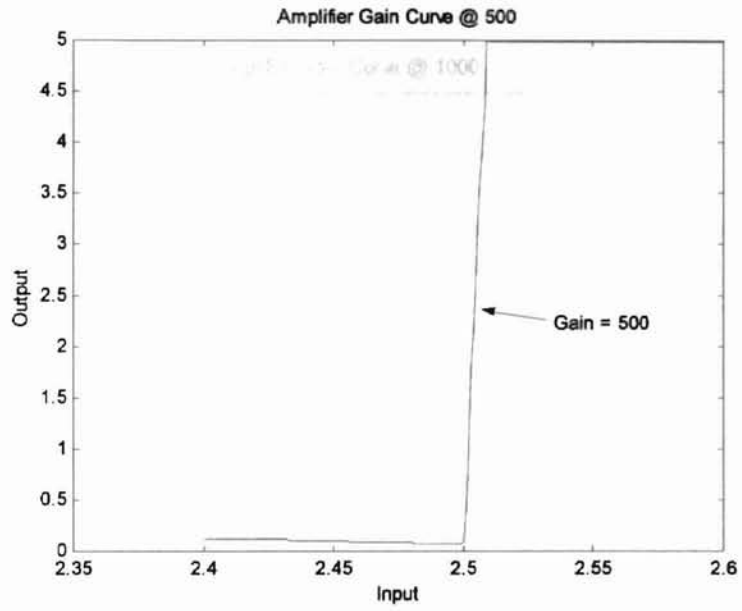


figure 3.7c Amplifier gain curve (Gain=500)

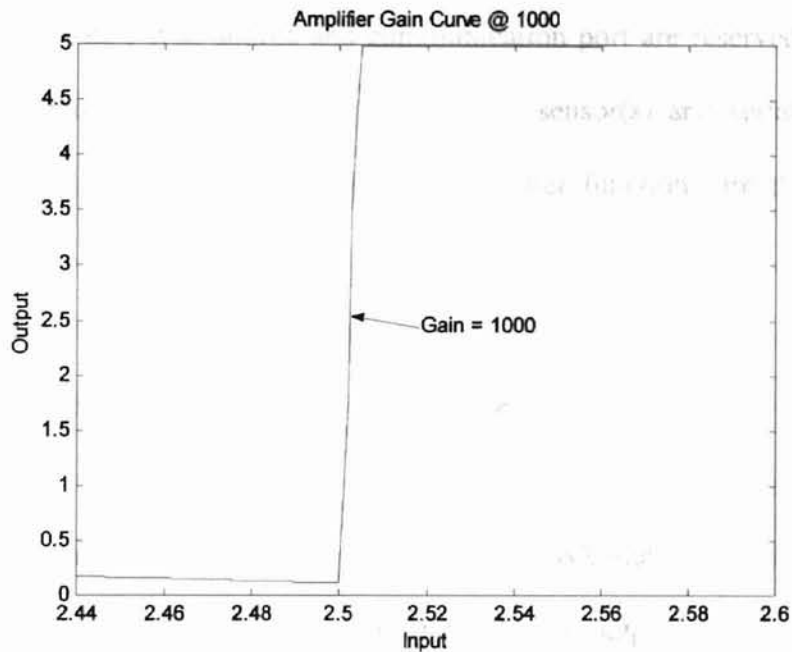


figure 3.7d Amplifier gain curve (Gain=1000)

The output offset, with zero input and a common mode voltage of 1.5V, is about 75mV at the maximum gain (1000). The equivalent input offset is 75uV. The safe operating range of input common-mode voltage is from 0.8V to 3.8V.

### 3.4 CPU and peripherals

The system is controlled by an 8-bit processor (PIC 16F874 from Microchip Inc.). This high-performance RISC CPU has several integrated peripherals and I/O ports. The controller has a built in Flash program memory with in-circuit programming capability. Besides volatile data RAM, an EEPROM data memory is also available for storing system calibration data and settings. The peripherals on chip include a 5 channel 10-bit ADC, two programmable PWM generators, serial communication ports and external



interrupt capability. The ADCs are used to sample the output of the amplifier and battery voltage. The PWM source and communication port are reserved for future upgrade to a closed loop control of the daughter board sensor(s) and serial link of data to a host computer. Further details about the controller functions are discussed in the software section.

### 3.5 Liquid Crystal Display (LCD) Interface

The main user interface device is a 16x2 matrix display (See appendix for data sheet). Various system conditions and RF level outputs are displayed on the LCD. The controller controls the display according to the real time state of the system. An 8-bit I/O port of the controller is reserved for data/instruction to the LCD apart from three control lines to set the bus state. The display is updated at 10Hz.

### 3.6 Power management

The power for the complete system is derived from an external battery pack. Regulated 5V supply ( $\pm 4\%$  regulation) is generated by solid-state integrated DC-DC converter based on charge pumps (MAX619, chip from Maxim Integrated Products; see appendix for data sheet.). Separate converters generate 5V supplies for the analog section and digital sections. This reduces the noise transfer from the digital section to the amplifier and also reduces the loading for the DC-DC converter. The safe range of input

voltage is 2V to 3.6V. The maximum output current is 50mA. Refer to data sheet in appendix for detailed specifications.

### 3.7 User Interface

The HHPM prototype board has multiple display screens generated by events or either of buttons. The buttons are named Sw1 (switch 1) and Sw2 (switch2). An event of pressing a switch for at least half a second and releasing initiates an event driven by that switch. This is, from now on, denoted as <Sw>. For example, event of pressing and releasing switch-1 is denoted as <Sw1>.

The display shows current display page and button functions. The sequence of screens and button functions are described in detail.

#### 3.7.1 Main Page

The main page is displayed on Power-on. This page displays the title and version number of the prototype.

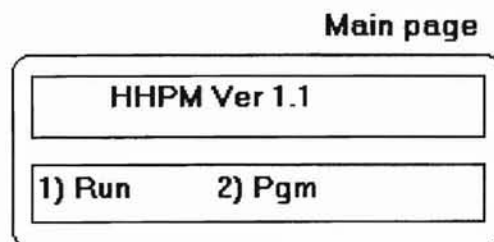


Figure 3.8 Main page display

Figure 3.8 shows the main page. <Sw1> brings up the RF power level display page and <Sw2> will switch the device to programming mode.

### 3.7.2 RF Level display page

RF level alarm and alarms can be  
adjusted with software changes

This page displays the RF level as a horizontal bar graph with various alarms active. The bottom line displays the current gain level set by the AGC (See Fig 3.9). The full-scale voltage level is displayed on the left side and gain of amplifier is showed on the right side.

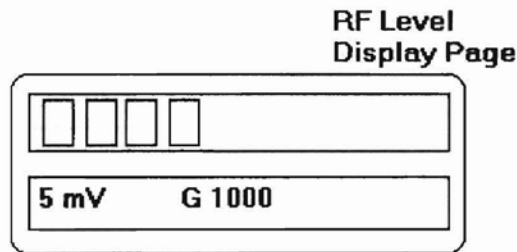


Figure 3.9 RF level display Page

<Sw1> in this page will lead to the battery level display and <Sw2> will take back to main page. Various alarms set for RF level warning are active in this page. When the input signal exceeds the range in the current gain level, the device switches to next gain.

Full Scale V	5 mV	10 mV	25 mV	50 mV
Amplifier gain	1000	500	200	100

Table 3.4 Gain levels versus full scale input

Table 3.4 shows the various gain levels corresponding to full-scale voltage on the display. The voltage step for every display increment is 1/12 of the full-scale value.

However, the controller records amplifier signals at 10bit accuracy and alarms can be triggered at an 8bit step size (10bit resolution is possible with software changes).

### 3.7.3 Battery Level Display Page

This display page shows a bar graph of battery voltage with in its operating range. Present settings display voltage from 2V to 3.2V with a 0.1V step.

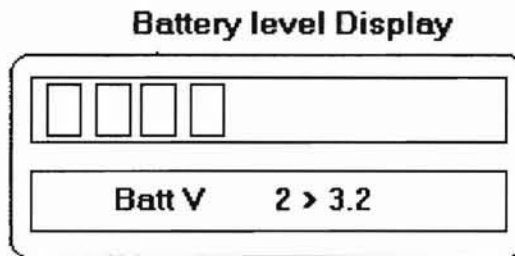


Figure. 3.10 Battery level display page

This page can be opened by <Sw1> from RF level page and changed back to RF level page by <Sw1> and <Sw2> will take back to the main page.

The figure 3.10 shows a sample page of battery level display. With the present settings, every matrix on the display is 0.1V. The Low-Battery beep is triggered at 2.5V (adjustable in software). When the battery voltage is below 2.2v, the “Low Battery” display appears which flashes (See figure 3.11), indicating that the battery voltage is low at an unsafe level.

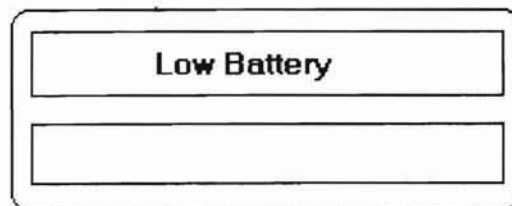


Figure 3.11 Low-battery warning

The Low-Battery page (Fig. 3.11) will be activated automatically from ANY page if the battery voltage goes below a safe level.

If the battery voltage to the system is greater than 3.7V (Maximum voltage supported by on board DC-DC converter, the system will display an 'Over Voltage' page (See figure 3.12) and normal functions are not accessible until the input voltage is below 3.7V.

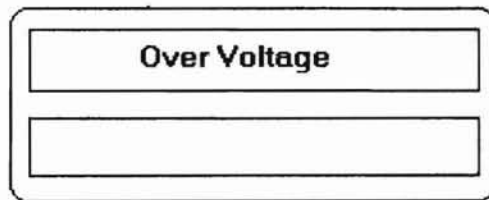


Figure 3.12 Over voltage warning page

The over voltage page is activated from ANY page if the input exceeds maximum voltage of 3.7V. Figure 3.13 shows the flow of events in the 'RUN' mode.

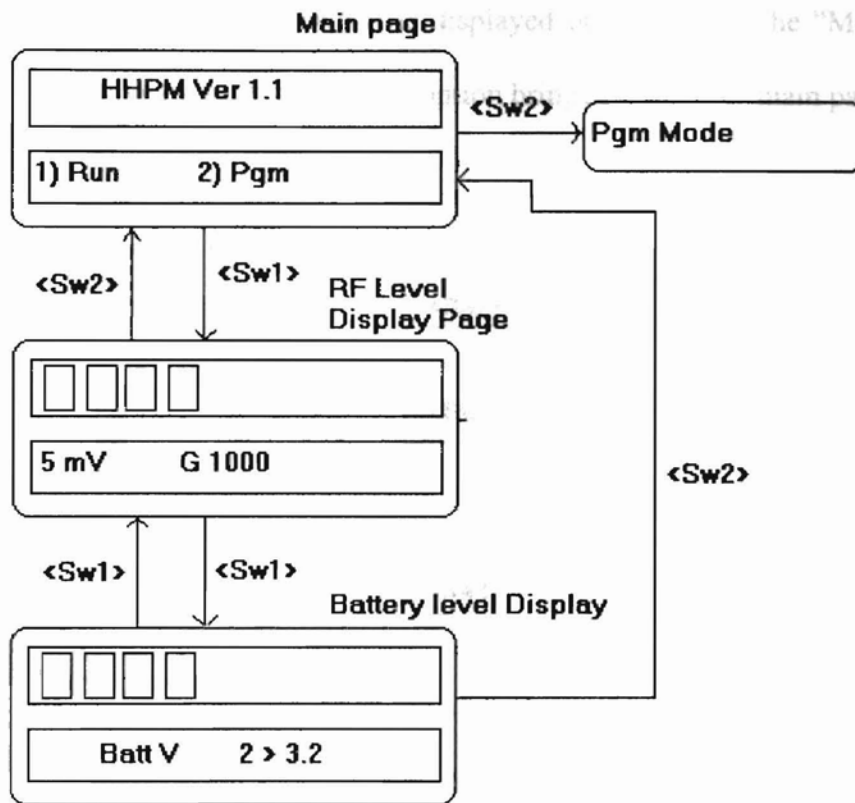


Figure 3.13 Flow of events in RUN mode

### 3.7.4 Program mode

The program mode is used to change user variables of the system. These settings will remain in memory as long as the system is powered. The next version of software will enable the settings to remain in the built-in EEPROM data memory. The present version allows the user to change input channel on the daughter board, turn 'off' or 'on' RF alarms. A page has been setup for the 'auto-zero' mode. This is currently not active, as it requires additional hardware on the daughter-board. The flow of events is shown in

Fig 3.14. The function of each switch is displayed on all pages. The “More >” option scrolls to next setup parameter and “Exit” option brings one back to main page.

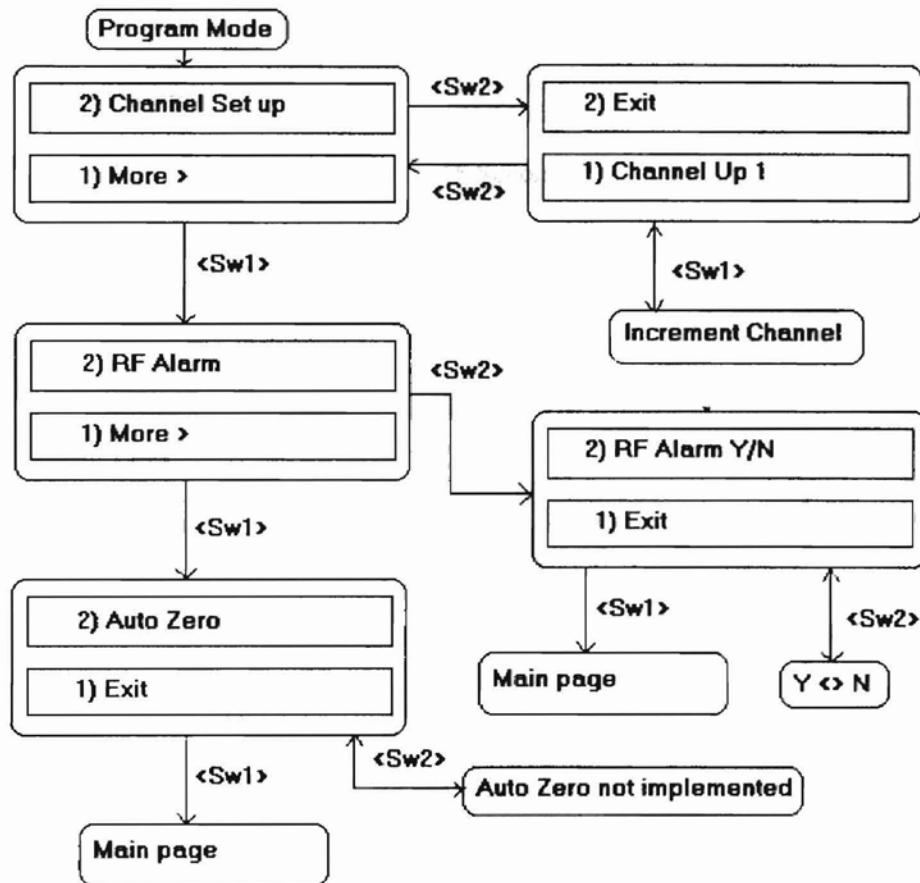


Figure 3.14 Flow of events in PROGRAM mode

The channel setup selects one of four channels on the daughter. As the channel is switched up the main board sends signals to the multiplexer on the daughter board, which selects the corresponding antenna.

The RF level warning alarms can be turned ON or OFF with the alarm setting. This controls all three alarms except battery level alarm that cannot be turned off.

### 3.8 Alarms

The system incorporates various audio alarms to indicate different states of warning. There are three RF level alarms and a low-battery alarm. Each of these alarms has a distinct pattern for the ease of recognition.

### 3.8.1 Low-Battery alarms

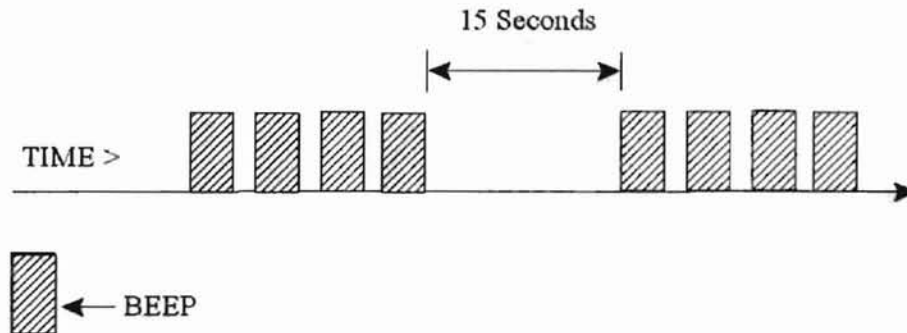


Figure 3.15 Low battery Alarm pattern

The Low battery alarm is triggered when the battery voltage falls below 2.5V. The pattern of the alarm is shown in Figure 3.15.

### 3.8.2 RF level alarms

There are three programmable alarm levels for sensor output voltage. The pattern of each alarm is distinct and has an increasing beep rate for each higher RF level. The beep pattern of alarms is shown in Fig 3.16.



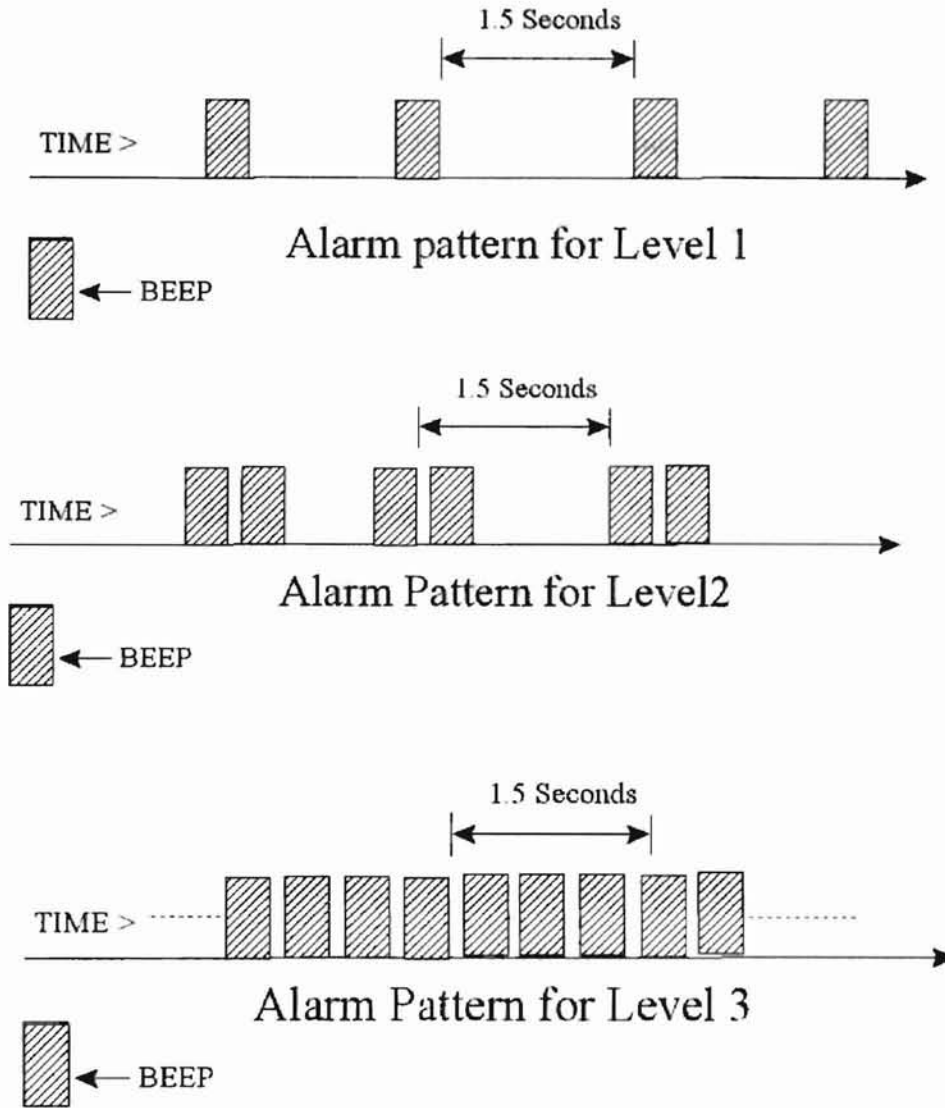


Figure 3.16 RF level alarm patterns

The trigger level for each alarm can be set independently in the software. This change is not accessible to the user and needs to be changed in the source code and reprogrammed (discussed later in this chapter). The alarms can be turned off in the program menu.

### 3.9 Software

The entire system is run by the firmware in the micro controller. The software is sectored into several subroutines, macros and interrupt services.

#### 3.9.1 Main loop

On power-up, the system does a self-setup. This includes clearing internal registers, initialize all the peripheral devices (internal and external), setup timers, and load initial conditions and defaults for all functions and events. The main loop includes subroutine calls. The highest level subroutines include:

- Logic and event sequencing
- ADC sampling for amplifier output at 200Hz and battery level monitoring.
- Update LCD from internal display RAM at 10Hz
- Update alarm setting to the pattern generator
- Sample user interface buttons with timed debounce.

The main flow of events in the algorithm is shown in figure 3.17. An internal timer generates a software interrupt. The interrupt service routine sets flag bits for all timed events in the algorithm at the required intervals. The timed events in the order of interval are:

- 250uS for alarm tone generation
- 5mS for ADC sampling

- 100mS for LCD updating
- 500mS for button debounce.
- Fractions and multiples of a second for alarm pattern generation.

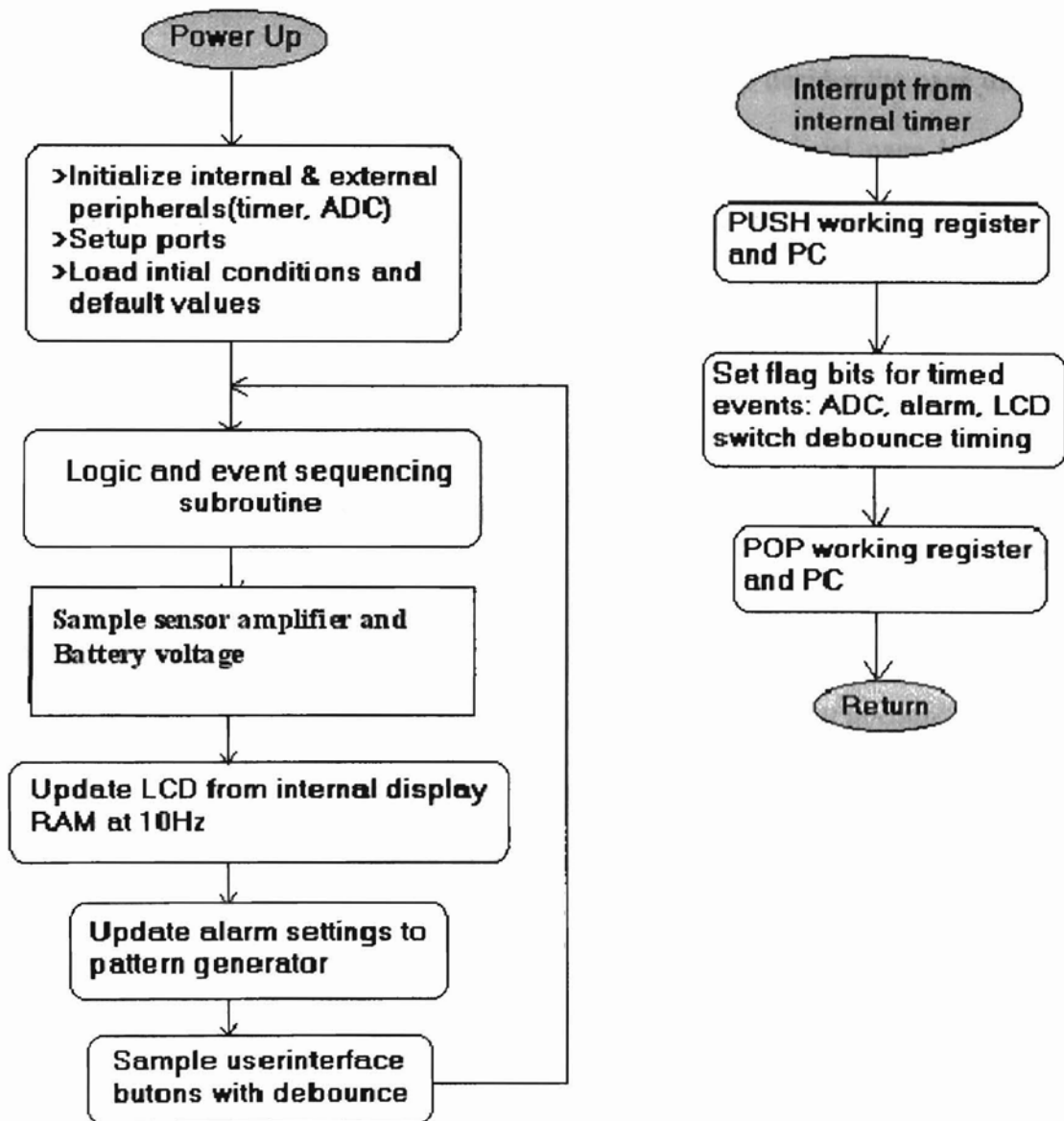


Figure 3.17 Main Algorithm

### 3.9.2 Logic control subroutine

The sequence of events and state of the system are decided in this subroutine. Various display pages are called according to buttons pressed. This subroutine calls other sub functions depending on the state of the system. The state decides the page displayed and its associated sub functions. For example, when the RF-level page is displayed, associated sub functions activated are automatic gain control, RF warning alarms etc.

### 3.9.3 Automatic gain control

The dynamic range of the RF power meter is enhanced by the automatic gain control. The controller constantly checks for the amplifier output and switches to the gain range giving maximum resolution. In order to reduce random switching from adjacent gain levels, when the signal level is at the point of transition, a small hysteresis window is provided at the transition. This reduces hunting between gain stages due to random signals and noise. Figure 3.18 shows AGC structure with hysteresis.

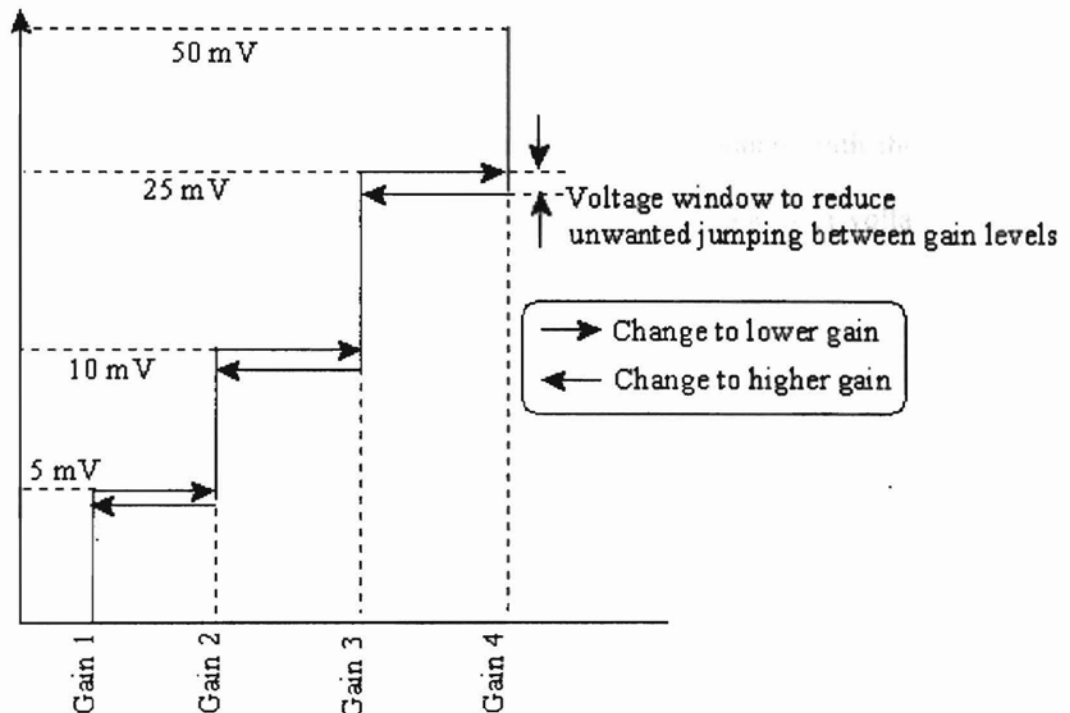


Figure 3.18 Automatic Gain Control

### 3.10 Adjusting software parameters

Certain parameters in the software may need to be changed to suit the working environment. The battery voltage warning levels and RF alarm levels can be changed in the software. These changes need to be reprogrammed into the controller through a programmer connected to a computer.

### 3.10.1 Changing low-battery alarm setting

There are three preset levels used in the software to compare with the sampled battery voltage: Low battery audio warning, Low battery cut off and over voltage. These are hexadecimal values stored as shown in Table 3.5.

<code>#define Lbat_alm</code>	<code>0X80 ; 2.5 Volts (Audio warning)</code>
<code>#define Lbat_wrn</code>	<code>0X70 ; 2.2 Volts (Visual warning)</code>
<code>#define Over_v</code>	<code>0XBD ; 3.7 Volts (Over voltage warning)</code>

Table 3.5 Block of code from line 38 through 40 in the source code.

A voltage of 0V to 5V on the battery is scaled as 00 to FF (Hexadecimal). The “Lbat\_alm” sets the Low-battery alarm level. Therefore 0X80 (0X denotes a hexadecimal number) denotes 2.5V on a 0 to 5V scale. “Lbat\_wrn” is the lowest voltage allowed on the battery before flashing “Low-battery” on the LCD. “Over\_v” sets the maximum voltage allowed. It is recommended that this setting remains unchanged unless the DC-DC converter on the board is changed.

### 3.10.2 Changing RF-power alarm levels

The RF alarm levels are set by two parameters for each of the three different alarms. The setting requires the gain level and the amplified sensor voltage at that gain level. For example, by default, the first level of alarm is set to trigger when input voltage exceeds half of full-scale in gain 4. Gain 4 is the highest gain (1000); the full scale of gain 4 is 5mV. Therefore half scale denotes 2.5 mV.

<code>#define rfa1_gn</code>	<code>0X04</code>	<code>;gain4 (5mV)</code>
<code>#define rfa1_lvl</code>	<code>0X80</code>	<code>;half scale 2.5 mV</code>
<code>#define rfa2_gn</code>	<code>0X03</code>	<code>;gain (10mV)</code>
<code>#define rfa2_lvl</code>	<code>0X80</code>	<code>;half scale 5mV</code>
<code>#define rfa3_gn</code>	<code>0X02</code>	<code>;gain (25mV)</code>
<code>#define rfa3_lvl</code>	<code>0X80</code>	<code>;half scale 12.5mV</code>

Table 3.6 RF alarm setting

'rfa1\_gn' is the gain level of the alarm 1 and 'rfa1\_lvl' is the hexadecimal value (0x00 to 0xFF) corresponding to the full scale value in that gain level (See table 3.6). Similarly, assigning 'rfa2\_gn' and 'rfa2\_lvl' with gain and hex values respectively can set alarm 2.

## CHAPTER 4

### INTEGRATED TEMPERATURE SENSOR

The recent trend in the VLSI industry is integration of the complete system on to a single substrate, this is also known as SOC (System on Chip). This would mean one substrate would contain the complete system from the signal source, for example, an antenna, sensor or transducer through signal conditioning, amplification, ADC and any required digital signal processing. This requires advanced fabrication techniques and superior circuit design and layout, taking into consideration signal-to-noise ratio and other critical aspects. A temperature sensor is a very common transducer used for a number of applications and frequently used for compensation of temperature drift. There are many designs and topologies for integrated temperature sensors based on available resources in a fabrication process [23]. A PN junction is a commonly used device to sense temperature because of its ready availability, ease of fabrication, consistency and robust device characteristics. This chapter explains the efforts to design and fabricate a low cost and linear temperature sensor based on a single PN junction [20]. Some of the key advantages of this topology are the independence to absolute value of bias current and the dependence on a fixed current ratio set by transistor-geometry and matching. The accuracy issues are limited to certain time difference between sampling, thermal time constants and settling explained in detail in this chapter.



#### 4.1 Principle of PN junction based temperature sensor

© 2019-2020, All rights reserved.

A PN junction exhibits temperature dependence in both forward and reverse biased conditions. The current equation for a forward biased diode is shown in equation (4.1). The forward thermal voltage  $V_t$  is a temperature dependent quantity (4.2).

$$I_D = I_S (e^{V_D/nV_t} - 1) \quad (4.1)$$

$$V_t = kT/q \quad (4.2)$$

Where  $I_D$  is the forward current in the diode,  $I_S$  is the reverse saturation current and  $V_D$  is the forward voltage across the diode. The thermal voltage  $V_t$  is directly proportional to the absolute temperature, where  $K$  is the Boltzmann's constant and  $q$  is the electron charge ( $1.6 \times 10^{-19}$  Coulomb). If the diode is maintained in forward bias by greater than  $4 V_t$ ,  $I_d$  will be much greater than  $I_S$  and equation (4.1) can be approximated as (4.3)

$$I_D = I_S (e^{V_D/nV_t}) \quad (4.3)$$

and rewritten as;

$$V_D = nV_t \ln \left[ \frac{I_D}{I_S} \right] \quad (4.4)$$

The reverse saturation current (or scale current) is a non-linear temperature dependent quantity [8].

$$I_S = Aqn_i^2 \left( \frac{D_p}{L_p N_D} + \frac{D_n}{L_n N_A} \right) \quad (4.5)$$

Equation 4.5 shows the relationship of  $I_s$  with the physical parameters of the diode, where  $A$  is the area of the junction,  $q$  is the electron charge and  $n_i$  is the carrier concentration which has a strong dependence on temperature. However, the complex relation of diode equation with temperature can be linearized by removing the dependence on  $I_s$ . This is achieved by dual-current sampling of diode voltage explained in the next section.

#### 4.1.1 Switched-current linearizing.

The nonlinear  $I_s$  dependence is removed by multiple sampling of the same diode voltage,  $V_D$ , at different known values of  $I_D$ . Consider Equation (4.4) at two known currents,  $I_{D1}$  and  $I_{D2}$ .

$$V_{D1} = nV_t \ln \left[ \frac{I_{D1}}{I_s} \right] \quad (4.6)$$

$$V_{D2} = nV_t \ln \left[ \frac{I_{D2}}{I_s} \right] \quad (4.7)$$

$$V_{D1} - V_{D2} = \Delta V_D = nV_t \ln \left[ \frac{I_{D1}}{I_{D2}} \right] \quad (4.8)$$

Equation (4.8) reveals that the reverse saturation current effects are removed from the relation and  $\Delta V_D$  is linearly dependent on temperature. If the current ratio  $I_{D1}/I_{D2}$  is fixed,  $\ln(I_{D2}/I_{D1})$  in the equation can be replaced by a constant 'M' resulting in (4.9). Therefore the absolute value of the bias current is not critical as long as the ratio is preserved.

$$\Delta V_D = nV_t M = n \frac{k}{q} MT \quad (4.9)$$

The assumptions for sensor accuracy is that temperature does not change while currents are switched and current ratio is known. These assumptions are readily achieved as long as any applied currents (power dissipated in the diode) remain small and sampling is done for short duration and hence, any rise in diode temperature fits to the required sensor accuracy. The accuracy is then maintained by switching test currents  $I_{D1}$  and  $I_{D2}$  at a rate much higher than the thermal time constant of the sensor. A source of static error is the inconsistency of current ratio which depends on transistor matching and is therefore process dependent.

#### 4.2 Circuit and diode Implementation

The sensor diode is implemented in an N-well. P+ and N-well implants form the diode (figure 4.1). The N-well and P-substrate forms a reverse-biased diode, as shown in figure 4.1. In order to eliminate the saturation currents across this reverse-biased stray diode, the N-well and substrate are electrically shorted as shown in the figure. This eliminates any potential across the stray diode and hence the reverse saturation current. The price of this advantage is that the sensor diode becomes ground-referred (since substrate is always at the lowest potential in the circuit), which is acceptable for this application.

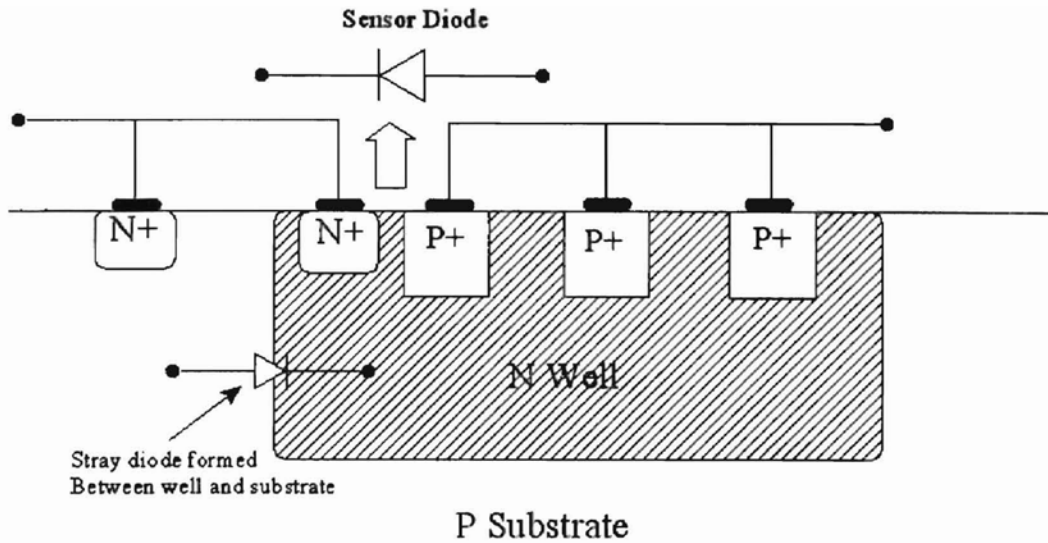


Figure 4.1 Implementation of sensor diode on the substrate

The circuit consists of a bank of current mirrors to provide the switched currents. A series of identical current mirrors are used to generate  $20I$  and  $I$ . The mirrors are cascoded P-types (See figure 4.2) to maintain accuracy by higher output impedances. An external bias sets the leg current for each of the current source. Since the absolute value of the current does not affect the accuracy, the currents don't have to be temperature independent as long as the diode operates in the log-linear region. A clock is used to switch the currents between  $I$  and  $20I$ .

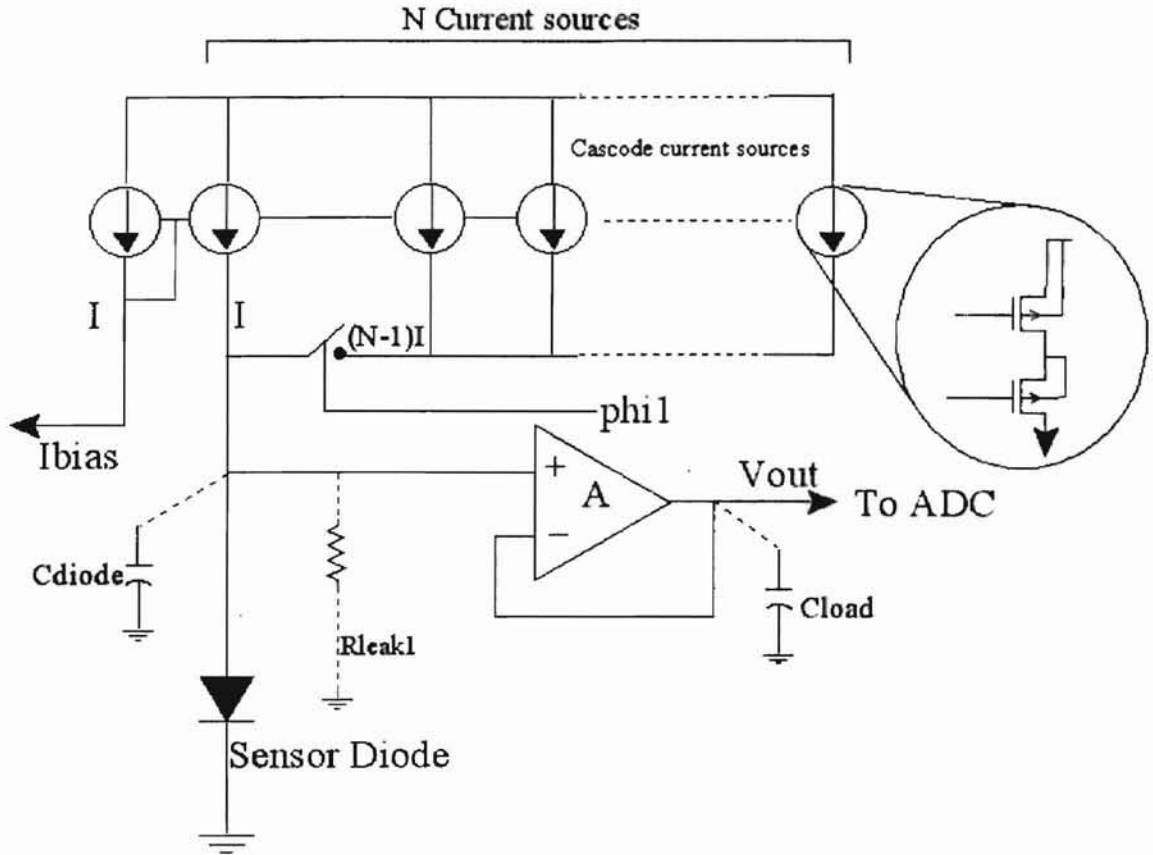


Figure 4.2 Implementation of temperature sensor

When the clock selects  $I_{D1}$  (switch is off), the drop across the diodes ( $V_{out}$ ) corresponds to the forward drop during the first cycle and is  $V_{D1}$ . During next clock cycle, when the switch is closed,  $NxI$  flows through the diode and  $V_{out}$  is  $V_{D2}$ . The ADC samples  $V_{D1}$  and  $V_{D2}$  at the end each clock cycle and the difference of  $V_{D1}$  and  $V_{D2}$  is the absolute temperature dependant voltage. All parasitic components and offset of the amplifier are a common-mode effect and will be eliminated when the difference is computed (Equation 4.10 ~ 4.12)

$$V_{D1} = V_{Diode(I)} + V_{offset} + \Delta V_{Parasitic} \quad (4.10)$$

$$V_{D2} = V_{Diode(N*I)} + V_{offset} + \Delta V_{Parasitic} \quad (4.11)$$

$$V_{Temp} = V_{D2} - V_{D1} = V_{Diode(N*I)} - V_{Diode(I)} \quad (4.12)$$

The time required for each clock state is set by the settling time of the input and output of the amplifier. The input node settles with an RC time constant set by the diode forward dynamic resistance and total capacitance of node (diode and amplifier input). The output settling is much faster since the amplifier drives the ADC, which has a much longer conversion time. This worst input time-constant is when diode current is minimum (when only I is selected). Equation set (4.13) estimates the worst time-constant.

$$\begin{aligned} \tau &= R_{forward} \times C_{inputnode} \\ R_{forward} &= V_{forward} / I_{forward} \\ R_{forward} &\cong 560mV / 800nA = 700k\Omega \\ C_{inputnode} &\cong 1pF \\ \tau &\cong 700nSec \end{aligned} \quad (4.13)$$

The settling time for a 9-bit accurate system is shown in equation (4.14)

$$\begin{aligned} t_{set} &= \tau \ln(2^{N+1}) \\ t_{set} &\cong 5\mu S \end{aligned} \quad (4.14)$$

Therefore the minimum sampling time required for each clock state is at least 5μS.

### 4.3 Self-heating Error Analysis

Self-heating of the diode during each clock cycle is a source of error for the temperature sensor. Heating takes place when diode dissipates power during forward bias

condition. The generated heat is forward current times the diode drop. Density of silicon is  $2.38 \text{ gm/cm}^3$  with a specific heat capacity of  $0.7 \text{ J/g K}$ . Considering the sensor to be on a silicon island of  $1\text{mm} \times 1\text{mm} \times 0.5\text{mm}$ , the mass of the sensor is  $1.164 \text{ mg}$ . The rise in temperature is as shown in equation 4.15

$$\Delta T = \frac{\Delta \text{Heat}(Q)}{\text{Mass} \times \text{Specificheat}} \times \text{time} \quad (4.15)$$

From equation 4.13, the minimum clock period is  $5\mu\text{S}$ . For worst-case consideration, consider a period of  $20\mu\text{S}$  (which includes I and 20I sampling). The rise in temperature from equation 4.14 is  $22\text{n K}$ . If the sensor makes 1000 temperature measurements per second, rise in temperature is  $22\mu\text{ K}$ . and the generated heat is  $18 \text{ n Joules}$ . Since the thermal conductivity of silicon is  $1.5 \text{ W/cm K}$ , a moderate thermally conducted substrate will result in a temperature raise of less than  $22\mu\text{K}$  if  $18\text{n Joules}$  is generated every second. Therefore worst error due to self-heating is and insignificant  $22\mu\text{K}$ .

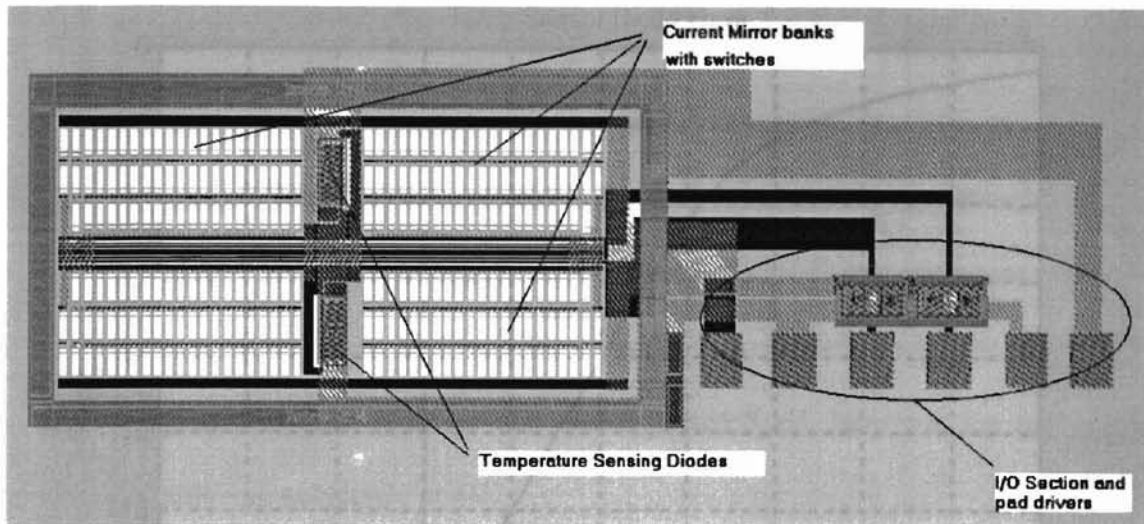


Figure 4.3 Layout of temperature sensor for AMI 1.2 micron process

#### 4.4 Test results of fabrication

The fabricated die was bonded into a standard package for testing the components and the sensor. Characteristic curves of the diode and current mirrors were plotted using the semiconductor parameter analyzer (HP-4155, Hewlett Packard Semiconductor Parameter Analyzer).

##### 4.4.1 Diode curves

The diode was tested to determine its log linear range to determine the proper operating values for  $I_{D1}$  and  $I_{D2}$ . Figure 4.4 shows a representative Log-linear curve of the diode fabricated in AMI 1.2 micron.



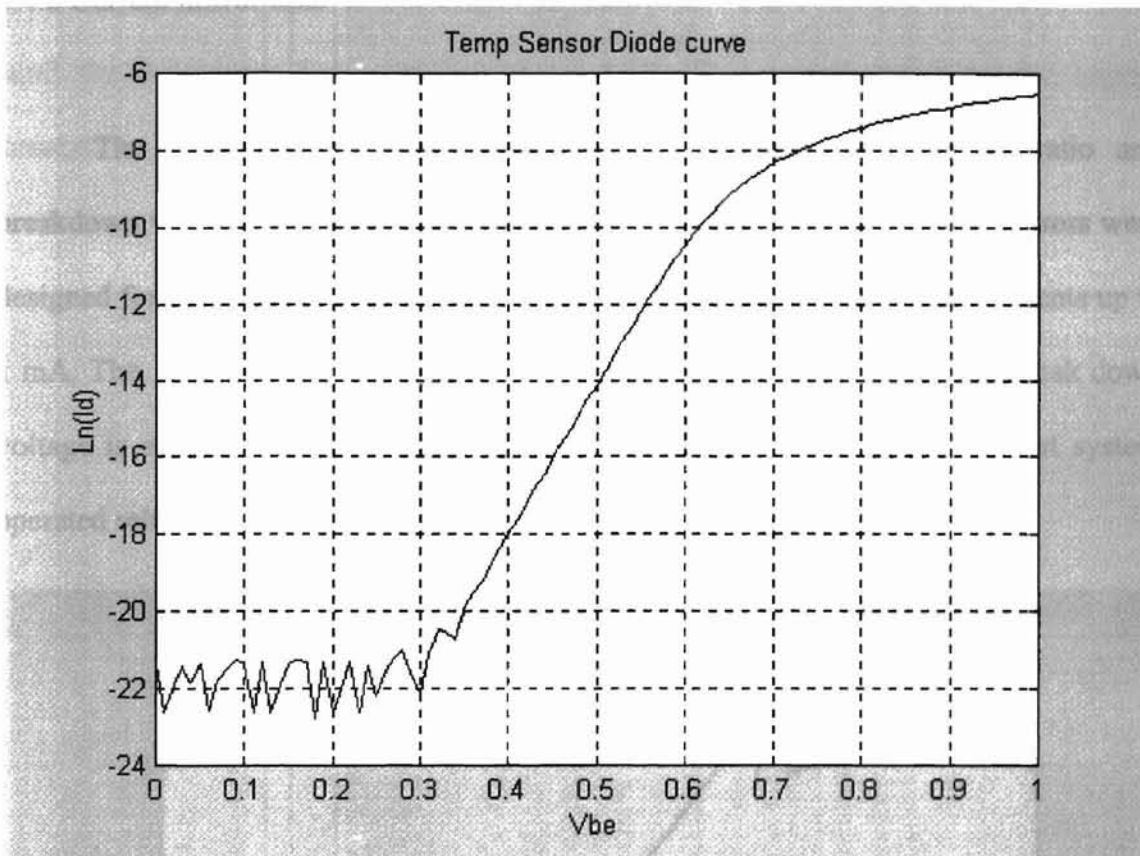


Figure 4.4 Log-linear curve of the sensor diode.

The ideality of the diode is found to be 0.96 from test data. The log-linear range accommodates a switching current ratio of 20. ( $1\mu\text{A}$  and  $20\mu\text{A}$ ). Hence the bias current for the sensor is  $1\mu\text{A}$ . This currents are valid for highest temperature of measurement the test setup, which was close to  $100\text{C}$ .

#### 4.4.2 Current mirror tests

The current mirror banks were tested to determine the current ratio and breakdown voltage. The results are plotted in figure 4.5 & 4.6. The cascode mirrors were designed for AMI 1.2 micron process, to work on 10V V<sub>dd</sub> with maximum currents up to 1 mA. The current ratio was 18.7, and the tested ratio had a -9% error. The break down voltage is around 4.5V and is lower than the expected 5.5V. However the test system operated reliably and accurately at 4V.

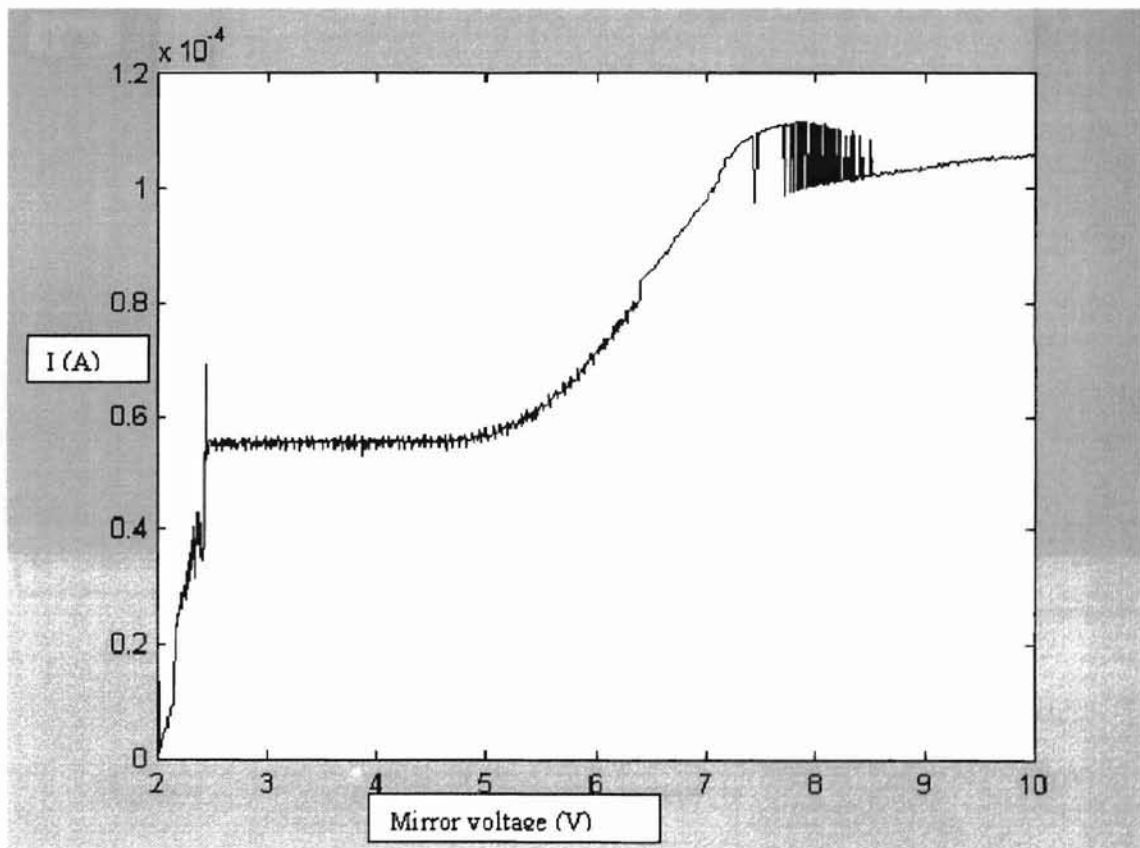


Figure 4.5 Current mirror plot at 55 $\mu$ A

The cascode mirrors start functioning at just below 2.5V. The currents hold their linearity until the breakdown begins at just above 4.5V. The currents begin to rise beyond breakdown voltage and the mirror bank fails to hold the design ratio of 20.

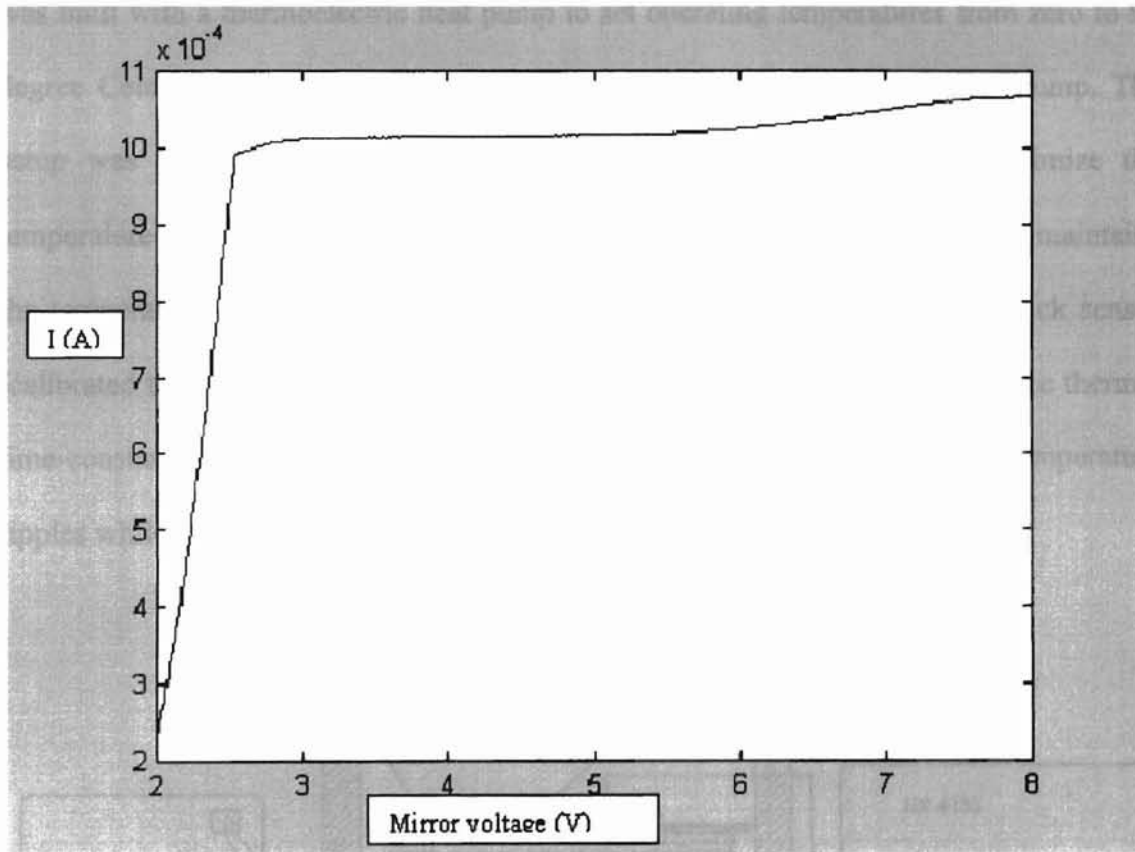


Figure 4.6 20x Current mirror plot at 55 $\mu$ A

### 4.3.3 Sensor tests

The complete sensor was tested for its functionality after each internal component was individually tested. The test setup is shown in figure 4.7. The temperature test setup was built with a thermoelectric heat pump to set operating temperatures from zero to 90 degree Celsius. The chip was thermally bonded to the thermoelectric heat pump. The setup was insulated thermally to reduce thermal leakage and hence minimize the temperature drift. The heat pump acts as a cooler or a heater. A PID controller maintains the temperature in the bath to an accuracy of 0.1 degree Celsius. The feedback sensor (calibrated thermistor) is bonded as close as possible to the heat pump to reduce thermal time-constant and hence reduce loop delay in the PID control to reduce temperature ripples while in close-loop control.

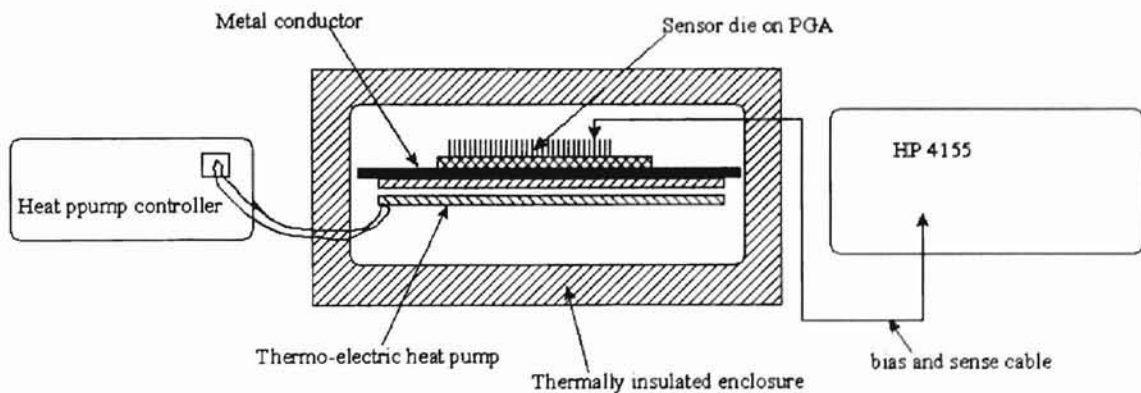


Figure 4.7 Test setup of the temperature sensor

The HP4155 parameter analyzer was used to generate bias currents and make measurements. A test algorithm was written and programmed HP4155 to generate  $I$  and sample diode forward voltage and then sample diode forward voltage at  $20 \times I$  while

maintaining the sensor at constant temperature. The sensor was tested from 3 degree Celsius to 86 degree Celsius for linearity. Figure 4.8 shows the test result of the sensor.

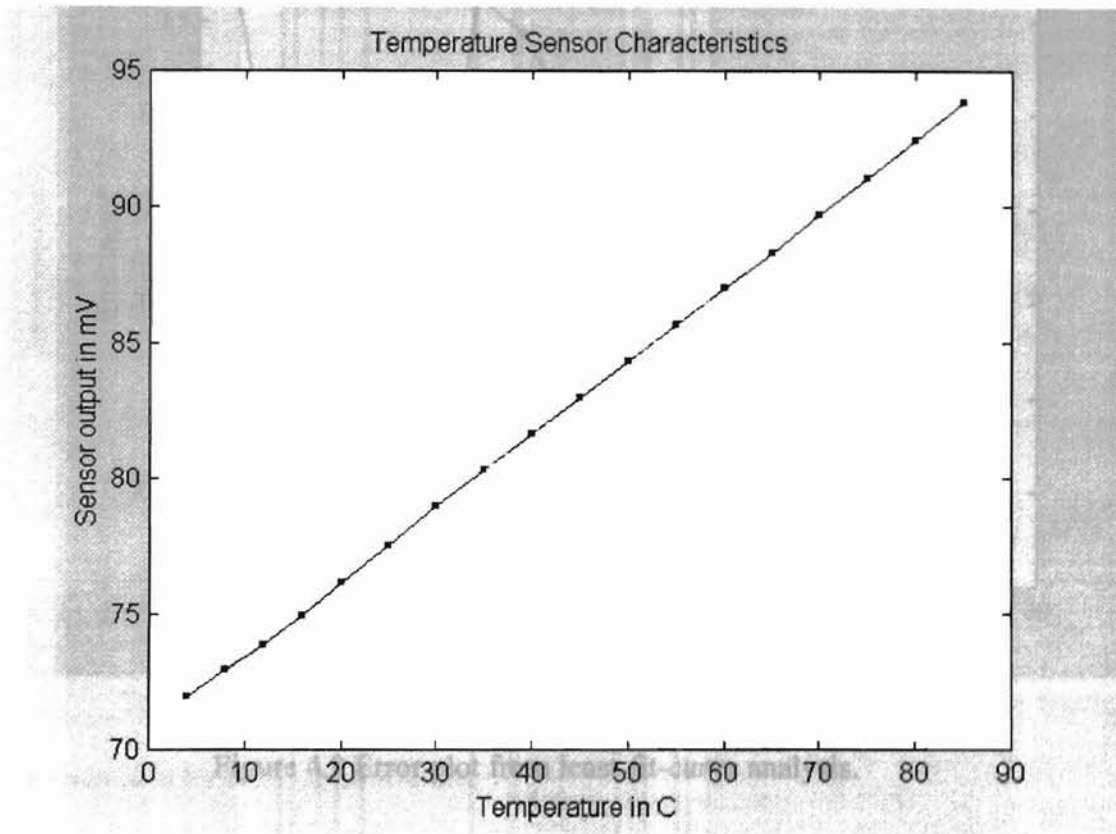


Figure 4.8 Temperature sensor characteristics

A linear regression analysis was conducted to determine the error and accuracy of the sensor. The error of the curve from the least fit curve was plotted (See figure 4.9).

The resulting error was random with a standard deviation of 0.0727 and a maximum value of  $148\mu\text{V}$ .

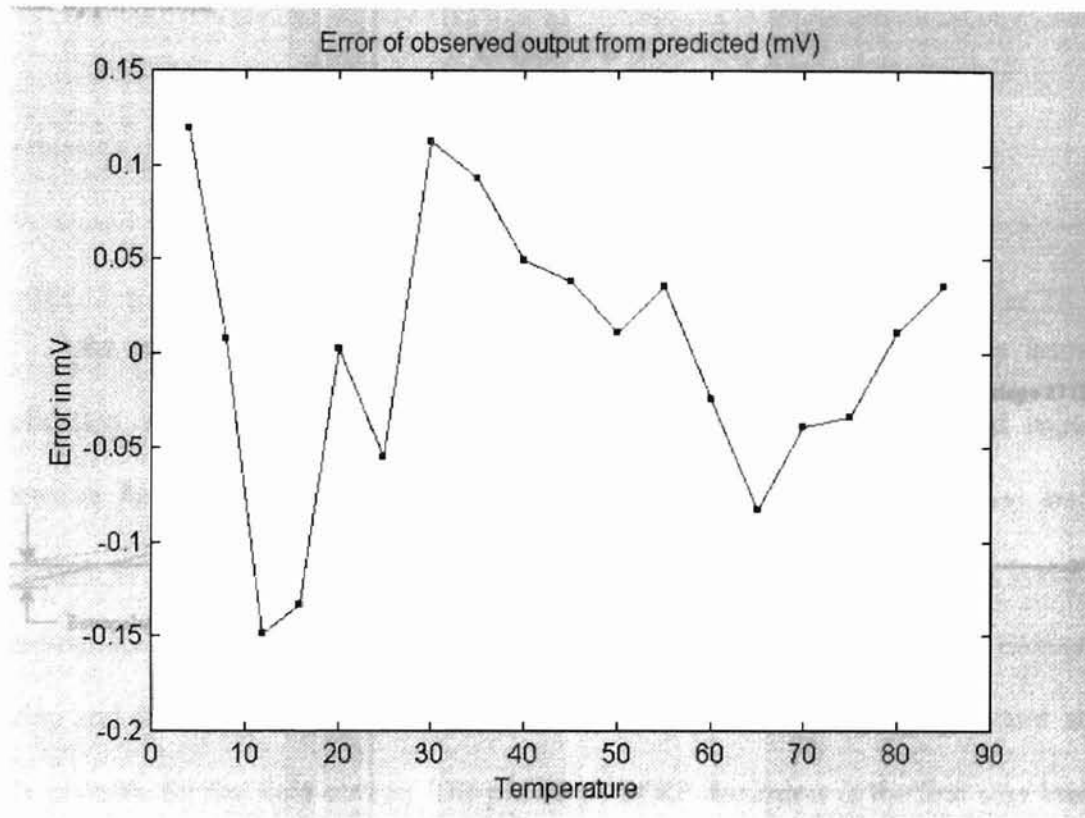


Figure 4.9 Error plot from least-fit-curve analysis.

Theoretically the sensor output converges to zero at  $-273\text{C}$  or zero Kelvin. The theoretical sensitivity for the sensor with an ideality factor of 0.96 for diode is  $248\mu\text{V}/\text{degree}$ . The measured sensitivity of the system is  $271\mu\text{V}/\text{degree}$  with an extrapolated offset of  $-3.23\text{mV}$  at zero Kelvin (figure 4.10). The resulting  $-8.5\%$  error in the sensitivity is due to following sources; 1) current mirror ratio, 2) accuracy of sensor temperature by the thermoelectric heater/cooler system and 3) low sampling rate of the

test setup. The  $-8.5\%$  error in the slope (see 4.4.2) is for all practical purpose due to the current-transfer-ratio of the mirror. The remaining error factors are not applicable in actual application.

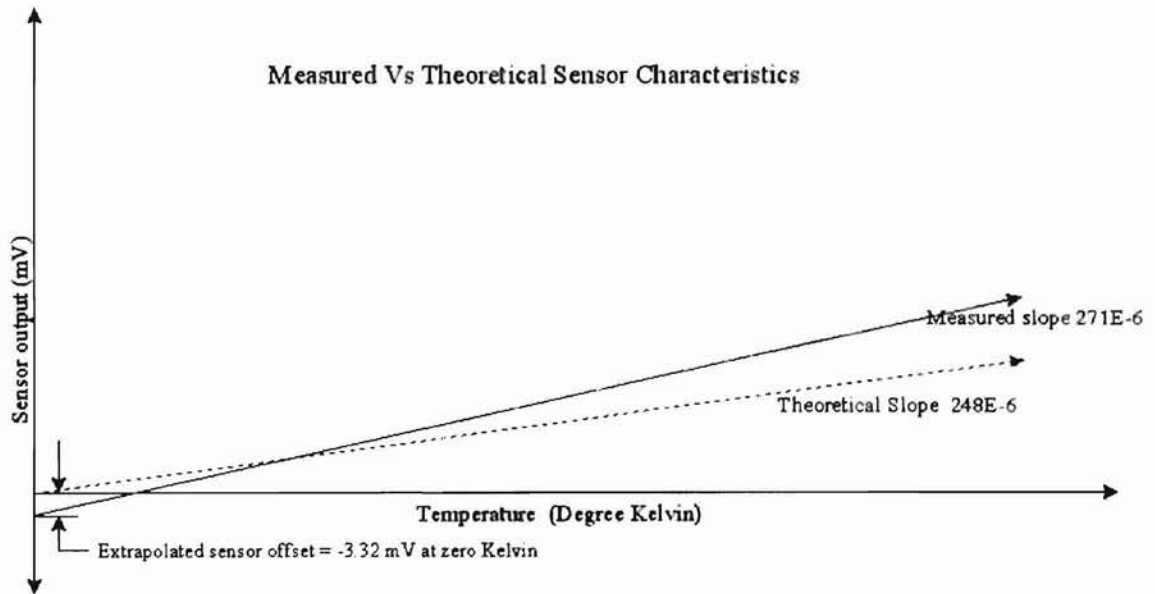


Figure 4.10 Comparison of actual Vs theoretical sensor curve

Test data shows that the current-transfer-ratio results in a  $-9.5\%$  error leaving  $1\%$  accountable by other listed sources.

## CHAPTER 5

### CONCLUSIONS

As explained in the introduction of this thesis, RF dosimetry has immense application and use in diverse fields, which has fueled the research and provided resources for this project. The objective of thesis effort, ie, to design and build a prototype as a step towards the integrated version, was successfully completed, tested and demonstrated with all intended features. The device forms a platform for convenient testing and demonstration of the micro-machined antennae on the daughter-board and is fully portable for the field-testing. The prototype of RF dosimeter is the first step towards a complete integrated version, which will be commercially viable. Complete or partial integration of the system will make it more power and space efficient.

Apart from thermopile sensors, other sensor topologies, including active device based sensors, can be considered for higher sensitivity and bandwidth. The prototype forms an ideal platform to evaluate such sensors and make changes to accommodate them for the future integrated versions. The diode sensor has the advantage of ease of fabrication and less complexity and also has a greater sensitivity ( $270\mu\text{V}/^\circ\text{K}$ ) than a polysilicon-aluminum thermocouple ( $110\mu\text{V}/^\circ\text{K}$ ) [22].

Some of the issues to be considered for the future versions would include a better power-supply rejection for the first stage of the amplifier. This will boost the over all



dynamic range. The usage of discrete components is the cause for slight mismatch and offset at the output of the amplifier. These problems can be solved in the integrated version, which will have better amplifier characteristics.

The future work on RF dosimeter must work to reduce the power consumption of the system by the use of efficient analog components and processor. The SNR of the system and hence the sensitivity will be enhanced by better sensors and low-noise integrated amplifiers. The integrated version will also lower the dependence on DC-DC converter since the devices can be rated at lower voltages, thereby reducing the number of cells required in the battery.

The software is designed anticipating future modifications and additional features. These features include the ability to interface with a host computer and accommodate the protocols for data transfer and also download instructions from the computer to configure the dosimeter. This will reduce hardware adjustments and tuning of dosimeter, instead, a graphical-user-interface based application on a host computer would setup and configure a dosimeter specific to a field application or sensor in a user-friendly fashion. The present version has built in hardware for an RS232 interface and only requires a standard level-shifter/buffer IC for interface with PC. An onboard non-volatile memory is needed to store the sampled data in the future versions. The present version has limited EEPROM memory and has capability to interface to serial PROM, which may be of future value.

A complete hardware prototype of RF dosimeter was built on a multi-layered PCB with all sections tested to function as designed. All the goals intended for the prototype of the RF dosimeter were met according to specifications and successfully

tested and demonstrated. This design and test phase towards the future integrated version of dosimeter has been a complete success.

The temperature sensor, investigated in this thesis, showed excellent results. The measured accuracy is  $271\mu\text{V}/^\circ\text{K}$  and the theoretical accuracy is calculated to be  $248\mu\text{V}/^\circ\text{K}$ . There is a 9% slope error in the characteristic curve of the sensor with the theoretical model. This error is predominantly due to mismatch in the current mirror bank. A source of dynamic error (resulting from finite  $\lambda$ ) results in lower-than-expected output impedance of the cascode mirrors. This results in drain voltage modulation of the mirrored current and hence error in the current ratio. Achieving better mirror accuracy and using better fabrication process and design can minimize these errors. Higher power-supply rejection ratio is desirable to make the sensor immune to variations in the supply voltage and RF injection. The delay between current sampling in the test setup is not an issue for actual application. The overall performance of the integrated temperature sensor is satisfactory and can find a variety of valuable applications as an absolute temperature sensor in portable devices, transducers in medical implants, substrate temperature measurements etc.

Future work will involve the development of a two-chip system for the dosimeter architecture, the first being the multiple sensor and the second being the analog conditioning with signal acquisition and controller.

## REFERENCES

- [1] N.H.E. Weate and K. Eshraghian, Principles of CMOS VLSI Design, A System Perspective, Santa Clara, CA, Addison-Wesley Publisher Ltd. 1993
- [2] Johnson, Howard W., High-speed Digital Design: a Handbook of black magic. Upper Saddle River, NJ: A simon & Schuster Company, 1993.
- [3] C.D. Motchenbacher and J.A. Connelly., Low Noise Electronic System Design, A Wiley-Interscience Publication.
- [4] David A. Johns and Ken Martin., Analog Integrated Circuit Design, John Wiley and Sons, Inc. 1997.
- [5] Tanner Tools. Pasadena, CA: Tanner Research, Inc. 1996
- [6] Christian C. Enz and Gabor C. Temes. Circuit Techniques for Reducing the Effects of Op-Amp Imperfections: Autozeroing, Correlated Double Sampling, and Chopper Stabilization, Proceedings of the IEEE, Vol. 84 No. 11, November 1996.
- [7] Kenneth R. Laker and Willy M.C. Sansen. Design of Analog Integrated Circuits and Systems. McGraw-Hill, Inc., 1994
- [8] Adel S. Sedra and Kenneth C. Smith. Microelectronic Circuits. Oxford University Press, 1998.

- [9] Dr. Louis Johnson, Class notes for ECEN 5263 VLSI Digital Circuit Design, Oklahoma State University 1997.
- [10] Venugopalan Pranesan, System Level Specifications for an Integrated RF Power Sensor, Oklahoma State University, May 2000.
- [11] Prasanna Weerasinghe, A 4-bit 1 GSPS Low-power Flash ADC with an Inherent Reference String, May 2000.
- [12] Quirino Balzano and Antonio Faraone, Human Exposure to Cellular Base Station Antennas, Motorola Florida Research Labs, FL.
- [13] Ralph A. Haller, FCC Regulations for Human Exposure to RF Fields, Fox Ridge Communications, Inc.
- [14] The Cellular Phone Scare, IEEE Spectrum, June 1993.
- [15] Anton Bakker and Johan H. Huijsing, Micropower CMOS Temperature Sensor with Digital Output, IEEE Journal Of Solid State Circuits, July 1996.
- [16] R. Lenggenhger, H. Baltes, Digest, International Conf. On Solid State Sensors and Actuators (TRANSDUCERS '95), Yokohoma, Japan, June, 1993.
- [17] Alan V. Oppenheim and Ronald W. Schafer, Discrete-time Signal Processing, Prentice-Hall, Inc. New Jersey, 1989.
- [18] Karl J. Astrom and Bjorn Wittenmark, Computer Controlled Systems, Prentice-Hall, Inc. New Jersey, 1984.

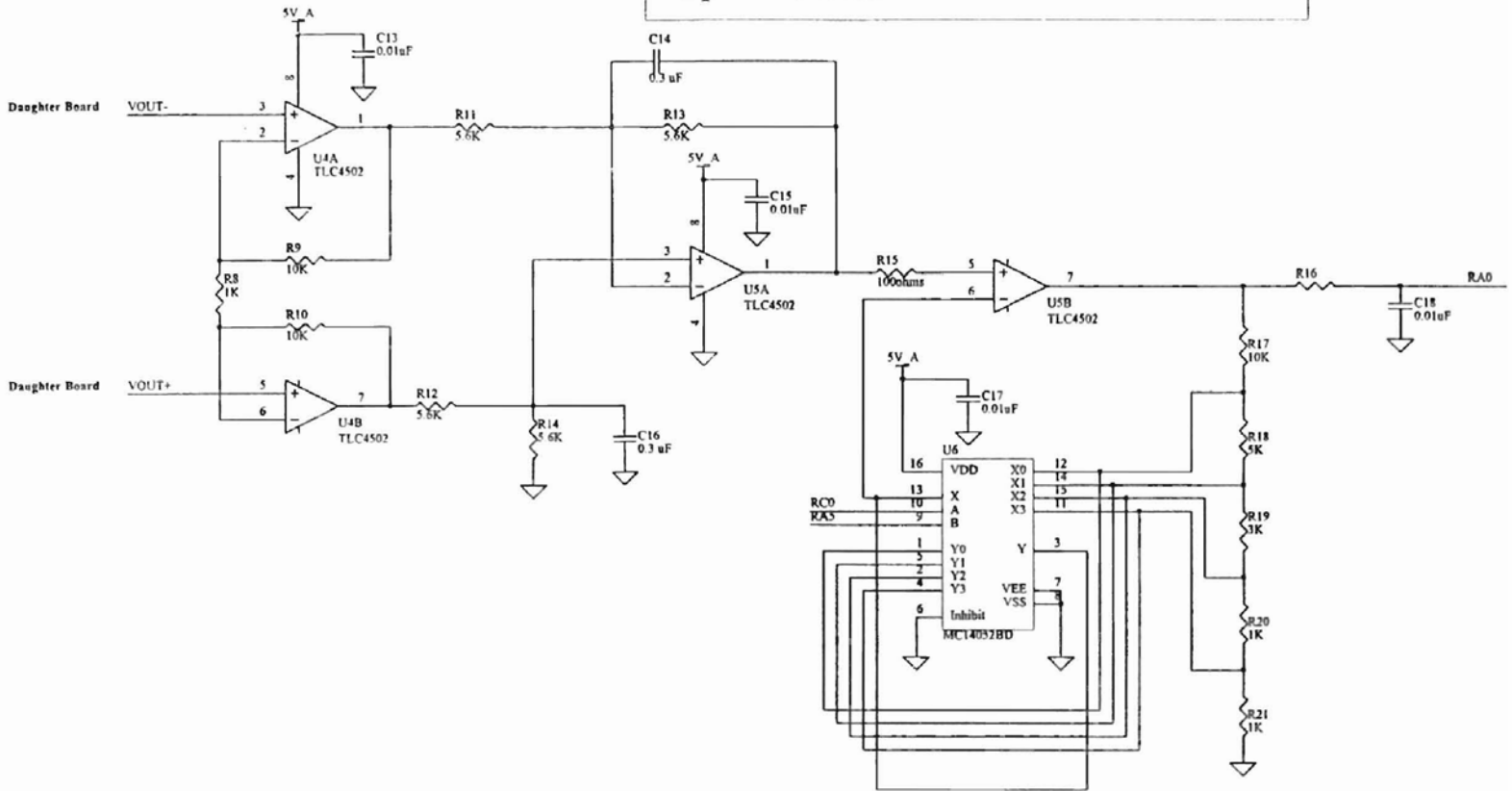
- [19] Chia-Ming Liu and Dr. Chris Hutchens, Low power decimation filter design for delta sigma converters, Advanced Analog VLSI Design Center, Oklahoma State University, 1999.
- [20] Raimundo Carlos, Serigo Daher, and Gurdip singh deep, senior member, IEEE, A Highly Linear Single p-n junction Temperature Sensor, IEEE Trans. On Instrumentation and measurements, Apr. 1994
- [21] Donald N. Williams, Multipurpose Power Sensor, ONR Review, SPAWAR Systems Center, San Diego, CA
- [22] Veljko Milanovi, Micromachined Broadband Thermocouple Microwave Power Sensors in CMOS technology, The George Washington University, Jan 1999.
- [23] Chi-Tsong Chen, Analog and digital control system design, Saunders College Publishing, 1993.
- [24] George T.A. Kovacs, Micromachined Transducers Source Book, WCB McGraw-Hill, Inc., Ney York, 1998.
- [25] Soon G. Lim, A 2KSPS 1mW Low power multibit delta sigma modulator with 16bit dynamic range, Oklahoma State University, May 1999.
- [26] T. Takken and D. Tuckerman, Integral Decoupling Capacitance Reduces Multichip Module Ground Bounce, IEEE Trans. On Electron Device. Vol. ED-32 No.12 pp79-84, 1993
- [27] Yuan Taur et al, CMOS Scaling into the Nanometer Regime, Proceeding of The IEEE, Vol.85, NO. 4, pp486-504, April 1997

- [28] Mohamed Ratni, Bernard Huyart, Louis Jallet, RF Power Detector Using a Silicon MOSFET, 1998 IEEE MTT-S Digest.

## APPENDIX A

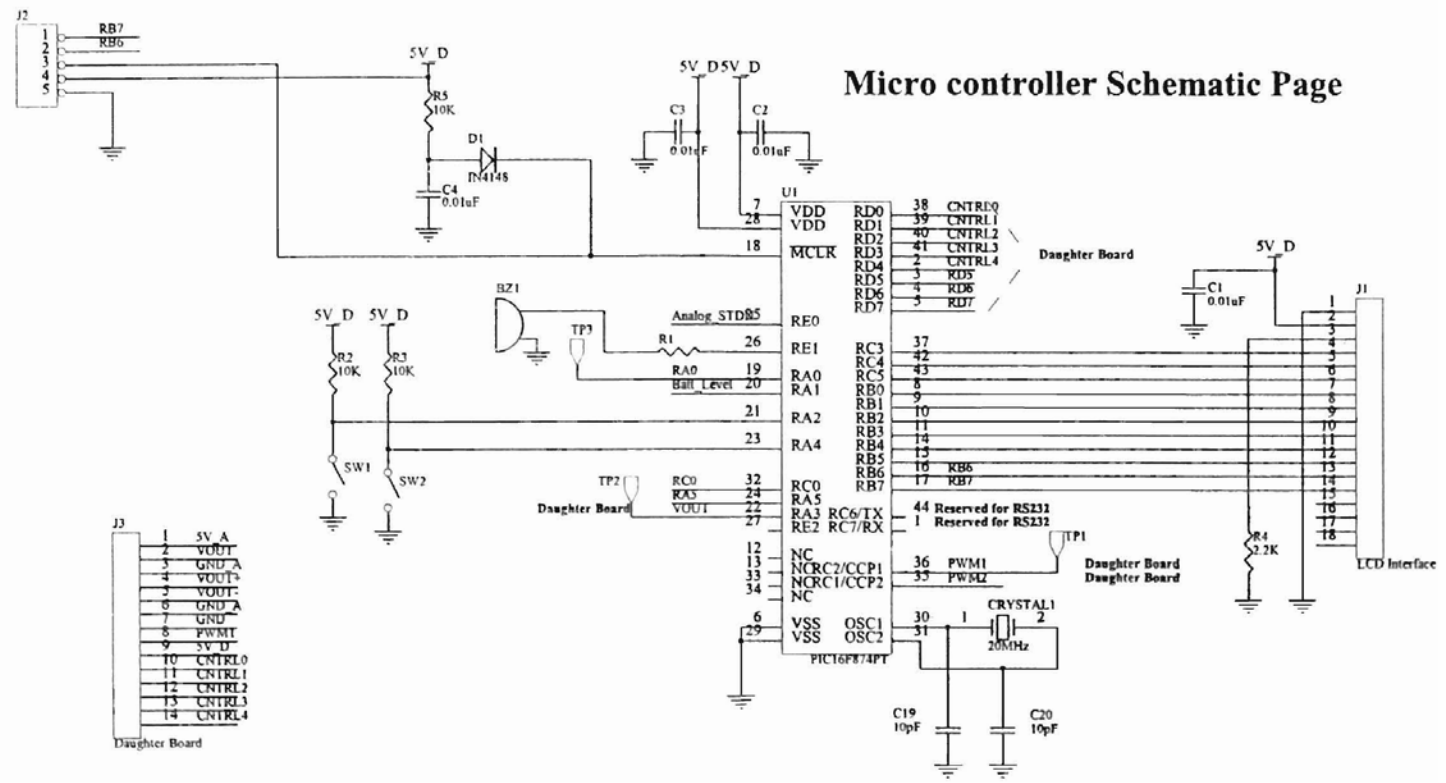
### DOSIMETER CIRCUITS AND DESIGN

### Amplifier Schematics

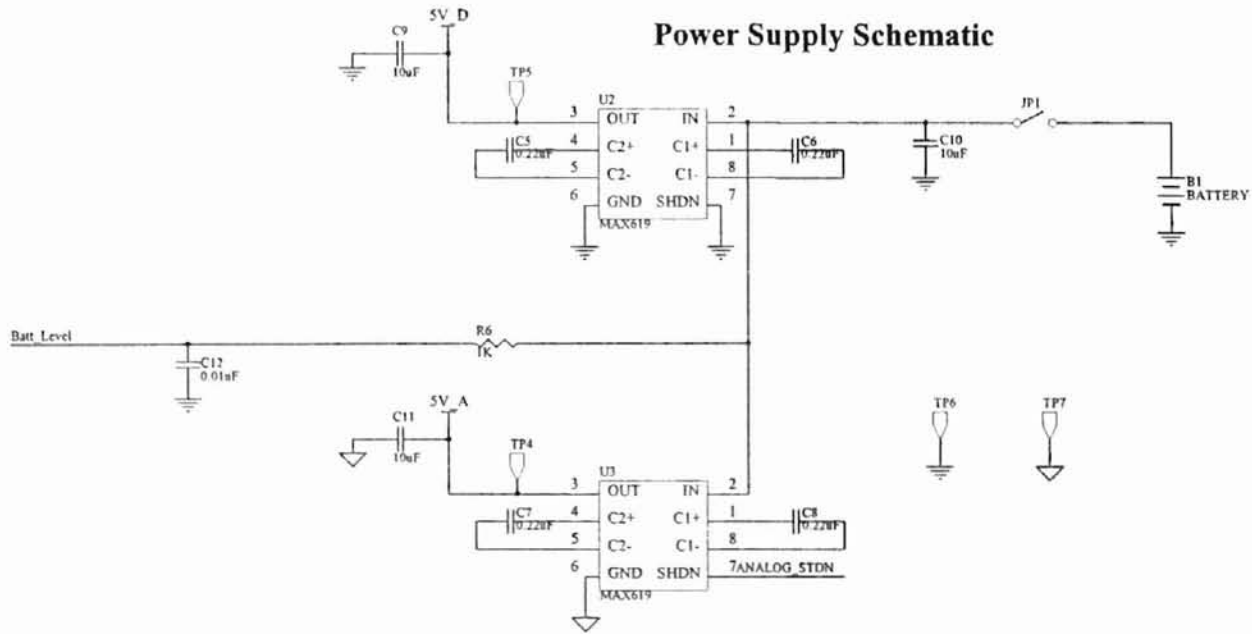




# Micro controller Schematic Page



### Power Supply Schematic



## AMPLIFIER DESIGN

The analog front-end amplifier is a three-stage configuration. First stage is a high input-impedance instrumentation amplifier. Second stage is differential buffer with a low pass filter at 100Hz. Final stage is a variable gain stage. The gain steps are discrete, which are digitally controlled by the micro-controller. All stages are built around TLC4502 (Texas Instruments Low-offset operational amplifier series)

Stage 1: Instrumentation Amplifier.

$$R9 = R10 = 10k$$

$$R8 = 1K$$

$$Gain = 1 + 2R9 / R8 = 21$$

Stage 2: Buffer with Low pass filter for 100Hz

$$R11 = R12 = R13 = R14 = 5.6k$$

$$C14 = C16 = 0.3\mu F$$

$$Gain = R13 / R11 = 1$$

$$\omega_{filter} = \frac{1}{2\pi RC} = 94.7Hz$$

Stage 3: Variable gain amplifier

$$R_{\text{total}} = R17 + R18 + R19 + R20 + R21 = 20K$$

$$\text{Gain} = R_{\text{Total}} / R_{\text{Selected}}$$

$R_{\text{Selected}}$	MUX input (Binary)	Amplifier Gain
10K	00	2
5K	01	4
2K	10	10
1K	11	20

$$\text{Total amplifier gain} = \text{Gain}_{\text{stage1}} * \text{Gain}_{\text{stage2}} * \text{Gain}_{\text{stage3}}$$

VITA<sup>2</sup>

Reghu Rajan

Candidate for the Degree of

Master of Science

Thesis: PROTOTYPE OF A HAND-HELD RF DOSIMETER BASED ON 8-BIT  
PROCESSOR AND AN INTEGRATED TEMPERATURE SENSOR

Major Field: Electrical Engineering

Biographical:

Personal Data: Born in Cochin, India, in 1974, the son of Kunnath R. Rajan and Rema Rajan.

Education: Completed High schooling from Model Technical Higher Secondary School, Cochin, India in 1991. Received Bachelor of Science degree in Electronics and Biomedical Engineering from Model Engineering College affiliated to Cochin University of Science and Technology, India, in August 1996. Completed the requirements for the Master of Science degree with a major in Electrical Engineering at Oklahoma State University in July 2001.

Experience: Worked with Wipro-GE medical systems as technical support engineer. Joined Grentel Technologies, India and served as circuit design engineer in the R&D from 1997 to December 1998. Employed by Oklahoma State University, School of Electrical and Computer Engineering as a graduate research assistant from May 1999 to present.

Professional Memberships: The Institute of Electrical and Electronics Engineers.